

# Revisiting $b \rightarrow c\tau\nu$ anomalies with charged Higgs boson

---

Nilakshi Das<sup>a</sup> Amit Adhikary<sup>b</sup> Rupak Dutta<sup>a</sup>

<sup>a</sup>*National institute of Technology Silchar 788010, Silchar, India*

<sup>b</sup>*Institute of Theoretical Physics, Faculty of Physics, University of Warsaw, Pasteura 5, PL 02-093, Warsaw, Poland*

*E-mail:* [nilakshi\\_rs@phy.nits.ac.in](mailto:nilakshi_rs@phy.nits.ac.in), [amit.adhikary@fuw.edu.pl](mailto:amit.adhikary@fuw.edu.pl),  
[rupak@phy.nits.ac.in](mailto:rupak@phy.nits.ac.in)

**ABSTRACT:** Recent experimental measurements on the anomalies observed in B meson decays have pointed towards the possibility of new physics. The LHCb collaboration has reported a significant deviation, exceeding  $3.2\sigma$ , from the predictions of the standard model. This discrepancy is observed in the combined measurement on the ratio of branching ratio  $R(D) - R(D^*)$  for the decays corresponding to  $B \rightarrow D\ell\nu$  and  $B \rightarrow D^*\ell\nu$  processes. Furthermore, the other observables, such as  $R_{J/\psi}$ ,  $P_\tau^{D^*}$ ,  $F_L^{D^*}$ , and  $R_{\Lambda_c}$  in the  $b \rightarrow c\ell\nu$  transition, have also exhibited noticeable deviations from the standard model predictions. Motivated by these anomalies in the  $b \rightarrow c\tau\nu$  transitions, we perform a log-likelihood fit incorporating new physics scalar couplings and explored the implications of a charged Higgs boson within a generic two Higgs doublet model. Our comprehensive analysis, focused on the  $\tau\nu$  and  $b\tau\nu$  final states, was performed using the High Luminosity run of the Large Hadron Collider (HL-LHC). We demonstrate the sensitivity of the collider search for a low-mass charged Higgs boson while considering the current experimental constraints on various  $b \rightarrow c\tau\nu$  flavor observables.

---

## Contents

<b>1</b>	<b>Introduction</b>	<b>2</b>
<b>2</b>	<b>Theoretical framework</b>	<b>5</b>
<b>3</b>	<b>Input Parameters</b>	<b>6</b>
<b>4</b>	<b>Results from model-independent analysis</b>	<b>7</b>
4.1	Fit procedure	7
4.2	Scalar coupling sensitivity to the flavor observables	8
4.3	Contour plots	9
<b>5</b>	<b>Model description</b>	<b>17</b>
<b>6</b>	<b>Collider analysis</b>	<b>18</b>
6.1	The $\tau_h\nu$ channel	19
6.2	The $b\tau_h\nu$ channel	24
<b>7</b>	<b>Collider prospect of flavor anomalies</b>	<b>29</b>
7.1	Constraining the Yukawa couplings	29
7.2	Constraining the flavor observables	31
<b>8</b>	<b>Summary and outlook</b>	<b>33</b>
<b>A</b>	<b>Detail of the generation cuts and production cross section of backgrounds</b>	<b>35</b>

---

# 1 Introduction

The Standard Model (SM) of particle physics stands as a robust and extensively tested theoretical framework that has successfully described a wide range of experimental observations. However, several phenomena and experimental measurements suggest that the Standard Model (SM) is an incomplete description of nature. Some of these observations include neutrino oscillations, the existence of dark matter, the imbalance between matter and anti-matter in the universe, and various flavor anomalies in particle decays. These observations collectively highlight the necessity for further research and investigations aimed at advancing our understanding of the fundamental laws of nature. The pursuit of new physics beyond the Standard Model is essential to address these unanswered questions and to provide a more comprehensive framework that can account for all known phenomena.

Significant indications of physics beyond the Standard Model (BSM) have emerged in various aspects, notably in the realm of  $B$  meson decays. In particular, consistent discrepancies have been observed in multiple decay channels involving the quark level transition  $b \rightarrow c \ell \nu$ , as manifested by deviations in branching ratios. Furthermore, deviations in Lepton Flavor Universality Violating (LFUV) observables have also been observed. LFUV observables compare the couplings of light leptons (e.g. electrons/muons) and tau leptons in  $b \rightarrow c$  transitions, thereby probing the universality of lepton interactions. Departures from the expected universality indicate the New Physics (NP) contributions in these transitions. Over the past decade, experimental measurements from collaborations such as Belle, BaBar, and LHCb have collectively provided a wealth of intriguing indications pointing towards NP in this sector. These measurements have consistently exhibited deviations from the predictions of the SM indicate the existence of novel phenomena. Therefore, these measurements also serve as motivation for the further investigations into physics beyond the SM.

The experimental measurements of the ratio of branching fraction,  $\mathcal{R}_{D^{(*)}}$  in  $b \rightarrow c \ell \nu$  transition are as follows:

$$R_{D^{(*)}} \equiv \frac{\mathcal{B}(B \rightarrow D^{(*)} \tau \bar{\nu})}{\mathcal{B}(B \rightarrow D^{(*)} (e, \mu) \bar{\nu})}. \quad (1.1)$$

Recent measurements from the BaBar [1, 2], Belle [3–5], and LHCb [6–9] collaborations have unveiled significant deviations in the observables  $\mathcal{R}_D$  and  $\mathcal{R}_{D^*}$  compared to the predictions of the SM. The world average [10], determined by the HFLAV (Heavy Flavor Averaging Group) collaboration, indicates a tension of  $1.98\sigma$  and  $2.15\sigma$  between the measured values of  $\mathcal{R}_D$  and  $\mathcal{R}_{D^*}$  and their respective SM expectations. Moreover, the combined world average exhibits a notable deviation of  $3.2\sigma$  [10] from the SM prediction, accompanied by a correlation of  $-0.37$  between  $\mathcal{R}_D - \mathcal{R}_{D^*}$ .

The LHCb collaboration has also performed measurements on the ratio of branching fractions in decays of  $B_c \rightarrow J/\psi \ell \bar{\nu}$ , which exhibits the analogous quark-level transition  $b \rightarrow c \ell \bar{\nu}$ . The discrepancy in  $R_{J/\psi}$

$$R_{J/\psi} = \frac{\mathcal{B}(B_c \rightarrow J/\psi \tau \bar{\nu})}{\mathcal{B}(B_c \rightarrow J/\psi (e, \mu) \bar{\nu})}. \quad (1.2)$$

is about  $2\sigma$  deviations [11] from SM prediction.

The LHCb collaboration recently reported the inaugural measurement of the semileptonic decay process  $\Lambda_b \rightarrow \Lambda_c^+ \tau^- \bar{\nu}$ , yielding a significant signal with a significance of  $6.1\sigma$  in May 2022 [12]. The measurement provides a determination for the LFUV ratio  $R_{\Lambda_c}$ , which is given by

$$R_{\Lambda_c} = \frac{\mathcal{B}(\Lambda_b \rightarrow \Lambda_c^+ \tau^- \bar{\nu}_\tau)}{\mathcal{B}(\Lambda_b \rightarrow \Lambda_c^+ (e, \mu) \bar{\nu}_\mu)} = 0.242 \pm 0.026 \text{ (stat.)} \pm 0.040 \text{ (syst.)} \pm 0.059. \quad (1.3)$$

Apart from the LFUV observables, there are other measurements in the context of  $B \rightarrow D^* \tau \nu$  decay that exhibit deviations from the SM prediction. Specifically, the  $\tau$  polarisation asymmetry, denoted as  $P_\tau^{D^*}$  [13, 14], and the longitudinal polarisation fraction of  $D^*$  meson, denoted as  $F_L^{D^*}$  [15], show a deviation of approximately  $1.5 - 1.6\sigma$  from the SM expectation. They are defined as follows

$$P_\tau^{D^*} = \frac{\Gamma^+(B \rightarrow D^* \tau \bar{\nu}_\tau) - \Gamma^-(B \rightarrow D^* \tau \bar{\nu}_\tau)}{\Gamma(B \rightarrow D^* \tau \bar{\nu}_\tau)}, \quad F_L^{D^*} = \frac{\Gamma(B \rightarrow D_L^* \tau \bar{\nu}_\tau)}{\Gamma(B \rightarrow D^* \tau \bar{\nu}_\tau)}. \quad (1.4)$$

It has been shown in Ref. [16] that the lifetime of the  $B_c$  meson plays a crucial role in determining the Lorentz structures of scalar New Physics (NP) interaction. In SM, the lifetime of the  $B_c$  meson ( $\tau_{B_c}$ ) sets a limit on the yet unmeasured branching ratio  $\mathcal{B}(B_c \rightarrow \tau \nu)$ , which should not exceed the total decay width of the  $B_c$  meson. This constraint has a significant effect on the couplings of scalar New Physics scenarios. The calculated value in SM is  $\tau_{B_c} = 0.52_{-0.12}^{+0.18}$  ps, obtained through operator product expansion [17, 18]. Importantly, this theoretical prediction is in good agreement with the experimental measurement of  $\tau_{B_c} = 0.507(9)$  ps [19].

The requirement that the branching fraction  $\mathcal{B}(B_c \rightarrow \tau \nu)$  remains less than or equal to 5% can be relaxed up to 30% when considering the upper bound of  $\tau_{B_c}$  [16]. However, more recent data from the LEP experiment at the Z peak has imposed a stricter constraint, demanding that  $\mathcal{B}(B_c \rightarrow \tau \nu)$  be less than or equal to 10% [20]. This constraint is considerably stronger than the one obtained from the  $B_c$  meson lifetime, which allowed for a  $\mathcal{B}(B_c \rightarrow \tau \nu)$  of up to

30%. Nevertheless, it is important to consider all possible uncertainties and a maximal value of  $\mathcal{B}(B_c \rightarrow \tau\nu) \leq 60\%$  is still a reasonable choice [21]. An extensive comparative assessment among the three distinct bounds of 10%, 30%, and 60% can be found in Ref. [21]. For the analysis of new physics scenarios in our paper, we adopt these three bounds for the branching fraction,  $\mathcal{B}(B_c \rightarrow \tau\nu)$ .

Numerous analyses [22–57], both model-independent and model-dependent, have been performed to investigate the possibility of NP explanations for the observed deviations in  $b \rightarrow c\ell\nu$  decays. These works have explored different NP scenarios in an attempt to explain these measured values, assuming that the deviations are not simply statistical fluctuations, underestimated theoretical errors, or systematic errors.

In this article, we investigate the type-III Two Higgs Doublet Model (2HDM) with generic flavor structure [58, 59], as a simple extension of the SM to explain the observed anomalies in LFUV observables. In the type-III 2HDM, both Higgs doublets couple to both up-type and down-type quarks, unlike the type-II 2HDM or the Minimal Supersymmetric Standard Model (MSSM). This model predicts a total of five Higgs states, including two CP even Higgs bosons ( $h, H$ ), one CP odd Higgs boson ( $A$ ), and two charged Higgs bosons ( $H^\pm$ ). Previous studies [26, 60–77] have shown that the charged Higgs boson ( $H^\pm$ ) in this type-III 2HDM can simultaneously explain the anomalies observed in  $R_D$  and  $R_{D^*}$ . This is in contrast to the type-II 2HDM or the MSSM [78–80], where it is challenging to account for both anomalies simultaneously. By considering the specific features of the type-III 2HDM, we aim to explore the parameter space and investigate the potential of the charged Higgs boson to provide a consistent explanation for the observed anomalies in various LFUV observables.

This paper is organized as follows: In section 2, we provide the theoretical formalism used for the analysis of NP effects and introduce the relevant formulae for the LFUV observables, referred to as flavor observables. The input values of the parameters used in our calculations are summarized in section 3. The results obtained from our model-independent analyses are presented in section 4. In section 5, we introduce the specific NP model considered in this study, namely the generic 2HDM. We discuss the theoretical framework and the features of the model that are relevant for explaining the observed deviations in the flavor observables. The collider analysis of the charged Higgs boson ( $H^\pm$ ) is explored in section 6. The constraints from collider analysis on the flavor observables are applied in section 7. Finally, we summarize our findings and conclude in section 8.

## 2 Theoretical framework

The effective Lagrangian for the quark-level transition  $b \rightarrow c\ell\nu$  in the presence of vector, scalar, and tensor new physics interactions can be expressed in the most general form [81, 82]:

$$\begin{aligned} \mathcal{L}_{eff} = & -\frac{4G_F}{\sqrt{2}}|V_{cb}|\left[ (1 + C_{LL}^V)\mathcal{O}_{C_{LL}^V} + C_{RL}^V\mathcal{O}_{C_{RL}^V} + C_{LR}^V\tilde{\mathcal{O}}_{C_{LR}^V} + C_{RR}^V\tilde{\mathcal{O}}_{C_{RR}^V} + C_{LL}^S\mathcal{O}_{C_{LL}^S} \right. \\ & \left. + C_{RL}^S\mathcal{O}_{C_{RL}^S} + C_{LR}^S\tilde{\mathcal{O}}_{C_{LR}^S} + C_{RR}^S\tilde{\mathcal{O}}_{C_{RR}^S} + C_{LL}^T\mathcal{O}_{C_{LL}^T} + C_{RR}^T\tilde{\mathcal{O}}_{C_{RR}^T} \right] + \text{h.c.} \end{aligned} \quad (2.1)$$

where,

$$\begin{aligned} \mathcal{O}_{C_{LL}^V} &= (\bar{c}_L\gamma^\mu b_L)(\bar{\ell}_L\gamma_\mu\nu_L), & \mathcal{O}_{C_{RL}^V} &= (\bar{c}_R\gamma^\mu b_R)(\bar{\ell}_L\gamma_\mu\nu_L), & \tilde{\mathcal{O}}_{C_{LR}^V} &= (\bar{c}_L\gamma^\mu b_L)(\bar{\ell}_R\gamma_\mu\nu_R), \\ \tilde{\mathcal{O}}_{C_{RR}^V} &= (\bar{c}_R\gamma^\mu b_R)(\bar{\ell}_R\gamma_\mu\nu_R), & \mathcal{O}_{C_{LL}^S} &= (\bar{c}_R b_L)(\bar{\ell}_R\nu_L), & \mathcal{O}_{C_{RL}^S} &= \bar{\ell}_R\nu_L\bar{c}_L b_R, & \tilde{\mathcal{O}}_{C_{LL}^S} &= \bar{\ell}_L\nu_R\bar{c}_R b_L, \\ \tilde{\mathcal{O}}_{C_{RL}^S} &= \bar{\ell}_L\nu_R\bar{c}_L b_R, & \mathcal{O}_{C_{LL}^T} &= \bar{\ell}_R\sigma_{\mu\nu}\nu_L\bar{c}_R\sigma^{\mu\nu}b_L, & \tilde{\mathcal{O}}_{C_{RR}^T} &= \bar{\ell}_L\sigma_{\mu\nu}\nu_R\bar{c}_L\sigma^{\mu\nu}b_R. \end{aligned} \quad (2.2)$$

In the effective Lagrangian for the  $b \rightarrow c\ell\nu$  transition, the Fermi coupling constant is denoted by  $G_F$  and  $|V_{cb}|$  represents the Cabibbo-Kobayashi-Maskawa (CKM) matrix element. The NP Wilson coefficients (WC) are denoted as  $C_{LL,RL}^{(V,S,T)}$  and  $C_{LR,RR}^{(V,S,T)}$ , where the superscripts  $(V, S, T)$  correspond to the vector, scalar, and tensor NP couplings, and the subscripts  $(LL, RL, LR, RR)$  refer to the chirality of the involved neutrinos. The left-handed neutrinos are associated with the coefficients  $C_{LL}^{(V,S,T)}$  and  $C_{RL}^{(V,S,T)}$ , which describe the effects of vector, scalar, and tensor NP couplings involving left-handed neutrinos. The right-handed neutrinos, on the other hand, are associated with the coefficients  $C_{LR}^{(V,S,T)}$  and  $C_{RR}^{(V,S,T)}$ . These Wilson coefficients parametrise the strength of the NP interactions and can be constrained by experimental measurements of flavor observables in  $b \rightarrow c\ell\nu$  transitions. By studying the values and constraints on these Wilson coefficients, one can probe different NP Lorentz structures and assess their compatibility with the observed deviations from the Standard Model predictions.

We define various flavor observables related to the  $b \rightarrow c\ell\nu$  transition as follows:  $R_D$  and  $R_{D^*}$  represents the ratio of the branching ratio in  $B \rightarrow D\tau\bar{\nu}$  and  $B \rightarrow D^*\tau\bar{\nu}$  decay. Similarly,  $R_{J/\psi}$  and  $R_{\Lambda_c}$  characterise the ratio of branching ratio in  $B_c \rightarrow J/\psi\tau\bar{\nu}$  and  $\Lambda_b \rightarrow \Lambda_c\tau\bar{\nu}$ , respectively. The polarisation fraction of  $\tau$  lepton and the longitudinal polarisation fraction of  $D^*$  meson are denoted as  $P_\tau^{D^*}$  and  $F_L^{D^*}$  in  $B \rightarrow D^*\tau\bar{\nu}$  decays, respectively. These observables, evaluated at the bottom quark mass scale  $m_b$ , are defined in terms of the scalar couplings associated with the  $b \rightarrow c\ell\nu$  transition as follows [83–85]:

$$\begin{aligned}
R_D &\simeq R_D^{\text{SM}} \left\{ 1 + 1.49 \operatorname{Re}[C_{\text{LL}}^{\text{S}\star} + C_{\text{RL}}^{\text{S}\star}] + 1.01 |C_{\text{LL}}^{\text{S}} + C_{\text{RL}}^{\text{S}}|^2 + 1.01 |C_{\text{RR}}^{\text{S}} + C_{\text{LR}}^{\text{S}}|^2 \right\}, \\
R_{D^\star} &\simeq R_{D^\star}^{\text{SM}} \left\{ 1 + 0.11 \operatorname{Re}[C_{\text{RL}}^{\text{S}\star} - C_{\text{LL}}^{\text{S}\star}] + 0.04 |C_{\text{LL}}^{\text{S}} - C_{\text{RL}}^{\text{S}}|^2 + 0.04 |C_{\text{RR}}^{\text{S}} - C_{\text{LR}}^{\text{S}}|^2 \right\}, \\
P_\tau^{D^\star} &\simeq \frac{R_{D^\star}^{\text{SM}}}{R_{D^\star}} P_{\tau,\text{SM}}^{D^\star} \left\{ 1 + 0.23 \operatorname{Re}[C_{\text{LL}}^{\text{S}\star} - C_{\text{RL}}^{\text{S}\star}] - 0.07 |C_{\text{LL}}^{\text{S}} - C_{\text{RL}}^{\text{S}}|^2 + 0.07 |C_{\text{RR}}^{\text{S}} - C_{\text{LR}}^{\text{S}}|^2 \right\}, \\
F_L^{D^\star} &\simeq \frac{R_{D^\star}^{\text{SM}}}{R_{D^\star}} F_{L,\text{SM}}^{D^\star} \left\{ 1 - 0.25 \operatorname{Re}[C_{\text{LL}}^{\text{S}\star} - C_{\text{RL}}^{\text{S}\star}] + 0.08 |C_{\text{LL}}^{\text{S}} - C_{\text{RL}}^{\text{S}}|^2 + 0.08 |C_{\text{RR}}^{\text{S}} - C_{\text{LR}}^{\text{S}}|^2 \right\}, \\
R_{J/\psi} &\simeq R_{J/\psi}^{\text{SM}} \left\{ 1 - 0.1 \operatorname{Re}[C_{\text{LL}}^{\text{S}\star} - C_{\text{RL}}^{\text{S}\star}] + 0.04 |C_{\text{LL}}^{\text{S}} - C_{\text{RL}}^{\text{S}}|^2 + 0.04 |C_{\text{RR}}^{\text{S}} - C_{\text{LR}}^{\text{S}}|^2 \right\}, \\
R_{\Lambda_c} &\simeq R_{\Lambda_c}^{\text{SM}} \left\{ 1 + 0.34 \operatorname{Re}[C_{\text{LL}}^{\text{S}\star}] + 0.50 \operatorname{Re}[C_{\text{RL}}^{\text{S}\star}] + 0.53 \operatorname{Re}[C_{\text{LL}}^{\text{S}} C_{\text{RL}}^{\text{S}\star}] + 0.33 (|C_{\text{LL}}^{\text{S}}|^2 + |C_{\text{RL}}^{\text{S}}|^2) \right. \\
&\quad \left. + 0.53 \operatorname{Re}[C_{\text{RR}}^{\text{S}} C_{\text{LR}}^{\text{S}\star}] + 0.33 (|C_{\text{RR}}^{\text{S}}|^2 + |C_{\text{LR}}^{\text{S}}|^2) \right\}, \\
\mathcal{B}(B_c \rightarrow \tau \bar{\nu}) &\simeq \mathcal{B}(B_c \rightarrow \tau \bar{\nu})_{\text{SM}} \left\{ |1 - 4.35(C_{\text{LL}}^{\text{S}} - C_{\text{RL}}^{\text{S}})|^2 + |4.35(C_{\text{RR}}^{\text{S}} - C_{\text{LR}}^{\text{S}})|^2 \right\}
\end{aligned} \tag{2.3}$$

In our analysis, the Wilson coefficients mentioned in the previous discussion are defined at the renormalization scale of  $m_b$ . The computation of the ratio of branching fraction  $R_D$  and  $R_{J/\psi}$  involves the utilisation of specific form factors. For  $R_D$ , we employ the lattice QCD form factor as provided in Ref. [86], while for  $R_{J/\psi}$ , we make use of lattice QCD form factors as described in [87]. To calculate the observables  $R_D^\star$ ,  $P_\tau^{D^\star}$ , and  $F_L^{D^\star}$ , we utilise the Heavy Quark Effective Theory (HQET) form factors from [88]. Similarly, for the evaluation of  $R_{\Lambda_c}$ , we employ lattice QCD form factors [89].

### 3 Input Parameters

For transparency, we provide a comprehensive overview of the input parameters utilised in our calculations in Table 1. The masses of various hadrons and leptons, along with the relevant quark masses, are shown at the renormalization scale  $\mu = m_b$ . It is important to note that the uncertainties associated with the mass parameters and decay lifetimes of the hadrons are not taken into consideration in this analysis. However, we rigorously account for the uncertainties arising from the input parameters pertaining to the form factors and the CKM matrix element  $|V_{cb}|$ . These uncertainties play a significant role in our computations and are duly incorporated to ensure a comprehensive analysis.

Parameters	Values	Parameters	Values
$m_{B^-}$	5.27931	$m_{B_c}$	6.2751
$m_{J/\Psi}$	3.0969	$m_{D^{*0}}$	2.00685
$m_{\Lambda_b}$	5.61951	$m_{\Lambda_c}$	2.28646
$\tau_{B_c}$	$0.507 \times 10^{-12}$	$f_{B_c}$	0.434(0.015)
$\tau_{B^-}$	$1.638 \times 10^{-12}$	$m_{D^{*0}}$	2.00685
$\tau_{\Lambda_b}$	$(1.466 \pm 0.010) \times 10^{-12}$	$m_{B_c^*}$	6.332
$m_{B_c}$	6.272	$m_\tau$	1.77682
$m_e$	$0.5109989461 \times 10^{-3}$	$m_c$	0.91
$m_b$	4.18	$G_F$	$1.1663787 \times 10^{-5}$
$V_{cb}$	0.0409(11)		

**Table 1:** Input parameters required for the analysis [19]. Masses are quoted in units of GeV and lifetimes are shown in units of second.

## 4 Results from model-independent analysis

### 4.1 Fit procedure

To explore the implications of new physics, we perform a  $\chi^2$  fit by considering the experimental and theoretical measurements of various flavor observables such as  $R_D$ ,  $R_D^*$ ,  $P_\tau^{D^*}$ ,  $F_L^{D^*}$ ,  $R_{J/\psi}$ , and  $R_{\Lambda_c}$ . We provide a comprehensive table, Table 2, that presents the numerical inputs for these observables. We examine the consistency of the obtained results with other pertinent observables, including the branching ratio of  $B_c$  meson,  $\mathcal{B}(B_c \rightarrow \tau \bar{\nu})$  and the upper limits evaluated from collider analysis, in the subsequent sections.

The definition of the  $\chi^2$  fit function is as follows:

$$\chi^2 \equiv \sum_{i,j} (O^{\text{theory}} - O^{\text{exp}})_i \text{Cov}_{ij}^{-1} (O^{\text{theory}} - O^{\text{exp}})_j. \quad (4.1)$$

To perform the  $\chi^2$  fit and determine the best-fit values for the scalar couplings, we utilize the `iminuit` package [90, 91]. In this analysis, we minimize a negative log-likelihood function using a multivariate Gaussian probability density function. During the fitting procedure, we account for the correlation between the observables  $R_D$  and  $R_{D^*}$ , about  $-0.37$  [10], considering both the experimental errors and theoretical uncertainties. The scalar couplings are varied within the range of  $(-1, +1)$ , assuming them to be either real or complex. By minimising the negative log-likelihood function and considering the correlations and uncertainties, we aim to obtain the most probable values for the scalar couplings that best explain the observed deviations from the Standard Model predictions in the considered flavor observables.



	Standard Model prediction	Experimental measurement
$R_D$	$0.298 \pm 0.004$ [10, 86, 92–94]	$0.356 \pm 0.029$ [1–3, 10, 95]
$R_{D^*}$	$0.254 \pm 0.005$ [10, 96–99]	$0.284 \pm 0.013$ [1–4, 6–8, 10, 13, 14, 95]
$R_{J/\psi}$	$0.258 \pm 0.004$ [100, 101]	$0.71 \pm 0.17 \pm 0.18$ [11]
$P_\tau^{D^*}$	$-0.497 \pm 0.013$ [26]	$-0.38 \pm 0.51$ (stat.) $^{+0.21}_{-0.16}$ (syst.) [13, 14]
$R_{\Lambda_c}$	$0.324 \pm 0.004$ [102]	$0.242 \pm 0.026$ (stat.) $\pm 0.040$ (syst.) $\pm 0.059$ [12]
$F_L^{D^*}$	$0.46 \pm 0.04$ [32]	$0.60 \pm 0.08 \pm 0.035$ [15]
$\mathcal{B}(B_c \rightarrow \tau \bar{\nu})_{\text{SM}}$	$0.022$ [103]	—

**Table 2:** Current SM prediction and experimental measurements of  $R_D$ ,  $R_{D^*}$ ,  $R_{J/\psi}$ ,  $P_\tau^{D^*}$ ,  $R_{\Lambda_c}$ ,  $F_L^{D^*}$  and  $\mathcal{B}(B_c \rightarrow \tau \bar{\nu})$ .

## 4.2 Scalar coupling sensitivity to the flavor observables

In this section, we perform a fit of the scalar couplings  $C_{LL}^S$ ,  $C_{RL}^S$ ,  $C_{RR}^S$ , and  $C_{LR}^S$  to various measured observables, namely  $R_D$ ,  $R_{D^*}$ ,  $P_\tau^{D^*}$ ,  $F_L^{D^*}$ ,  $R_{J/\psi}$ , and  $R_{\Lambda_c}$ . Our analysis consists of three distinct scenarios. Firstly, we consider the “1D scenario” where we examine the effects of NP scalar couplings individually. This involves fixing all but one scalar coupling to zero and analysing the impact of that specific coupling on the observables. In the “1D scenario,” we further divide our analysis into two parts: we consider the case where the scalar coupling is assumed to be real and where it is taken as complex. Secondly, we explore the “2D scenario” where we investigate the effects of two NP scalar couplings simultaneously. Here, we vary two scalar couplings at once and assess their combined influence on the flavor observables.

- **Case-I :** In 1D real scenario, we get the best fit values of real scalar couplings as follows:

$$\begin{aligned}
C_{LL}^S &= 0.15, & C_{RL}^S &= 0.16, \\
C_{RR}^S/C_{LR}^S &= -0.51.
\end{aligned} \tag{4.2}$$

- **Case-II :** In 1D complex scenario, we obtain the following best fit values of complex scalar couplings.

$$\begin{aligned}
C_{LL}^S &= -0.67 - i \, 0.84, & C_{RL}^S &= 0.16 - i \, 6.4 \times 10^{-6}, \\
C_{RR}^S/C_{LR}^S &= -0.49 - i \, 0.14.
\end{aligned} \tag{4.3}$$

- **Case-III :** We perform a 2D parameter fit that gives the following best fit values of complex scalar couplings.

$$\begin{aligned}
(C_{LL}^S, C_{RL}^S) &= (-0.37 + i\,0, 0.48 + i\,0) , \\
(C_{LL}^S, C_{RR}^S/C_{LR}^S) &= (-0.67 - i\,0.5, -0.63 - i\,0.26) , \\
(C_{RL}^S, C_{RR}^S/C_{LR}^S) &= (0.16 - i\,1.6 \times 10^{-4}, \sim 0 + i\,0) , \\
(C_{RR}^S, C_{LR}^S) &= (-0.88 - i\,0.62, 0.50 + i\,0.45) .
\end{aligned} \tag{4.4}$$

### 4.3 Contour plots

We present the implications of our fit result in various planes, namely,  $R_D - R_{D^*}$ ,  $P_\tau^{D^*} - F_L^{D^*}$ ,  $R_D - R_{\Lambda_c}$ ,  $R_{D^*} - R_{\Lambda_c}$ ,  $R_D - R_{J/\psi}$  and  $R_{D^*} - R_{J/\psi}$  planes. In each figure, we display plots arranged in two rows. In the first row, the left plot represents the implications of the  $C_{LL}^S$  coupling, while the right plot shows the effects arising from the  $C_{RL}^S$  coupling. In the second row, the left plot shows the effect of the  $C_{RR}^S$  or  $C_{LR}^S$  coupling. Similarly, the right plot in the second row shows the implications of all 2D scenario coupling combinations such as  $(C_{RL}^S, C_{RR}^S/C_{LR}^S)$ ,  $(C_{LL}^S, C_{RL}^S)$ ,  $(C_{LL}^S, C_{RR}^S/C_{LR}^S)$ , and  $(C_{RR}^S, C_{LR}^S)$ . These figures offer a more comprehensive view of the parameter space by considering the interplay between different scalar couplings. In each figure, the experimental measurements are displayed as elliptical contours, and the uncertainties at  $1\sigma$ ,  $2\sigma$ , and  $3\sigma$  are represented by solid, dashed and dotted blue colored contours. The branching ratio of  $\mathcal{B}(B_c \rightarrow \tau \bar{\nu}) \leq 60\%$ ,  $30\%$  and  $10\%$  are shown with purple solid, dashed and dotted lines, respectively.

In Fig 1, we display the contour plots of  $R_D - R_{D^*}$ . Notably, it is evident that the SM prediction lies  $3\sigma$  away from the experimental measurement, as shown with black star. Here, one can observe the following:

- When considering the presence of the complex  $C_{LL}^S$  coupling, shown with green dot, the fit value of  $R_D - R_{D^*}$  almost coincides with the central values of the experimental measurements. This indicates a good agreement between the theoretical prediction and the data in this scenario. In case of the real  $C_{LL}^S$  coupling, shown with red circle, the fit value lies within the  $2\sigma$  contour of the experimental results. It is worth noting that the area below the upper bound of  $B_c \rightarrow \tau \nu$  is more favored [20].
- In the upper right plot, it is clearly visible that in the presence of both real and complex  $C_{RL}^S$  couplings, the value of  $(R_D, R_{D^*})$  coincide with each other. Further it is interesting that in both cases the  $(R_D, R_{D^*})$  value lies within the upper bound of  $B_c \rightarrow \tau \nu \approx 10\%$ .
- Similarly both the real and complex  $C_{RR}^S$  and  $C_{LR}^S$  show the similar fit results. Hence it can be seen that the fit values in the  $R_D - R_{D^*}$  plane lie within the  $2\sigma$  region of experimental measurement.

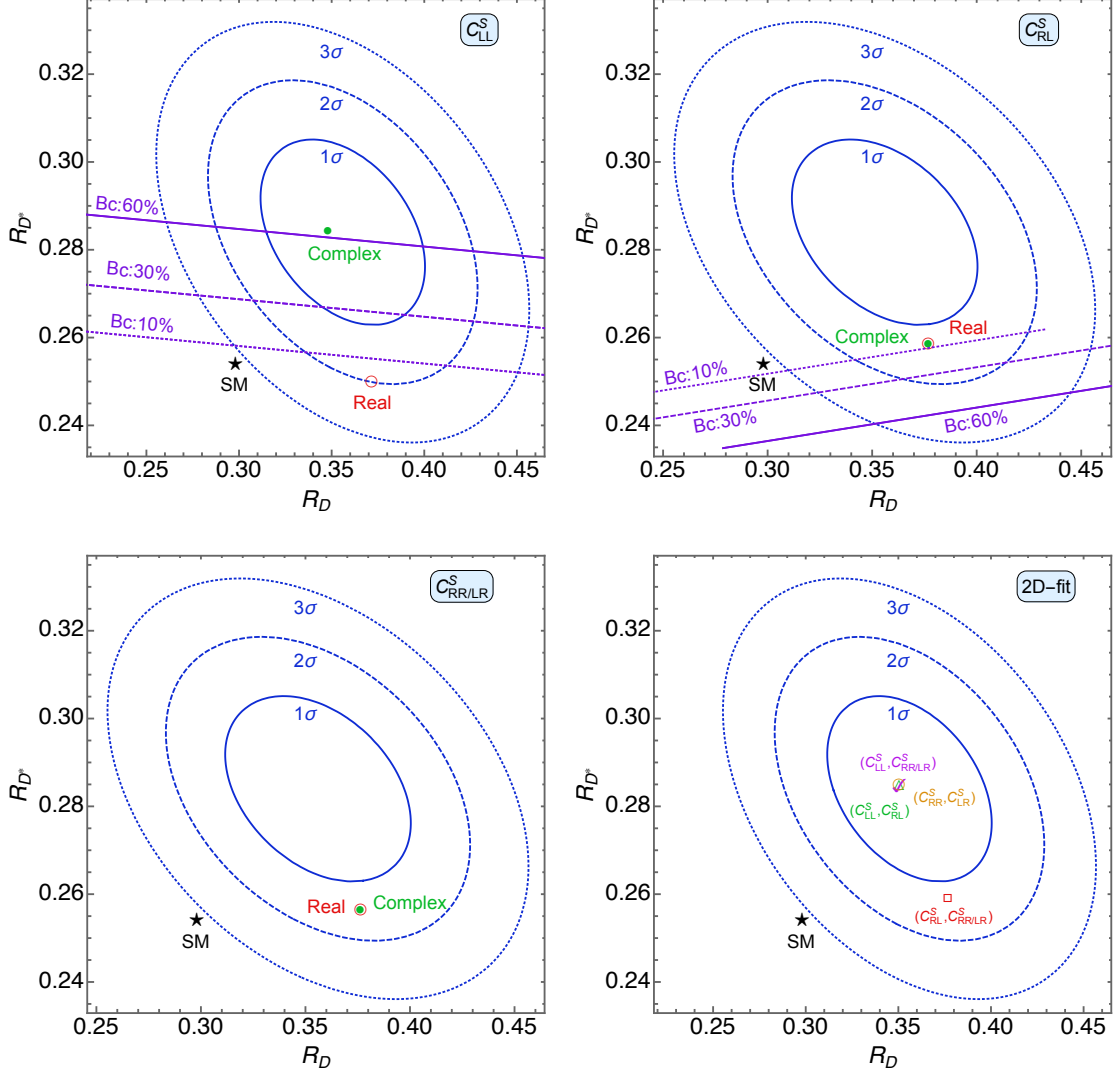


**Figure 1:** Allowed regions with best fit values of scalar couplings in the  $R_D - R_{D^*}$  plane. The  $1\sigma$ ,  $2\sigma$  and  $3\sigma$  contours are shown in solid, dashed and dotted blue color, respectively. The black star, red circle and green point represent the SM prediction, real and complex fit to the experimental measurement of  $R_D - R_{D^*}$ , respectively. The purple colored solid, dashed and dotted lines correspond to  $\mathcal{B}(B_c \rightarrow \tau \bar{\nu}) = Bc = 60\%$ ,  $30\%$  and  $10\%$ , respectively.

- In the presence of the  $(C_{RL}^S, C_{RR}^S/C_{LR}^S)$  coupling, the lower right plot clearly shows that the fit value in the  $R_D - R_{D^*}$  plane falls within the  $2\sigma$  experimental results. Furthermore, for the  $(C_{LL}^S, C_{RL}^S)$ ,  $(C_{LL}^S, C_{RR}^S/C_{LR}^S)$ , and  $(C_{RR}^S, C_{LR}^S)$  couplings, the fit values of  $(R_D, R_{D^*})$  coincides with the central value of the experimental measurement.

Now in Fig. 2, we show the results in  $P_\tau^{D^*} - F_L^{D^*}$  plane, for the mentioned three scenarios.

Here we observe that

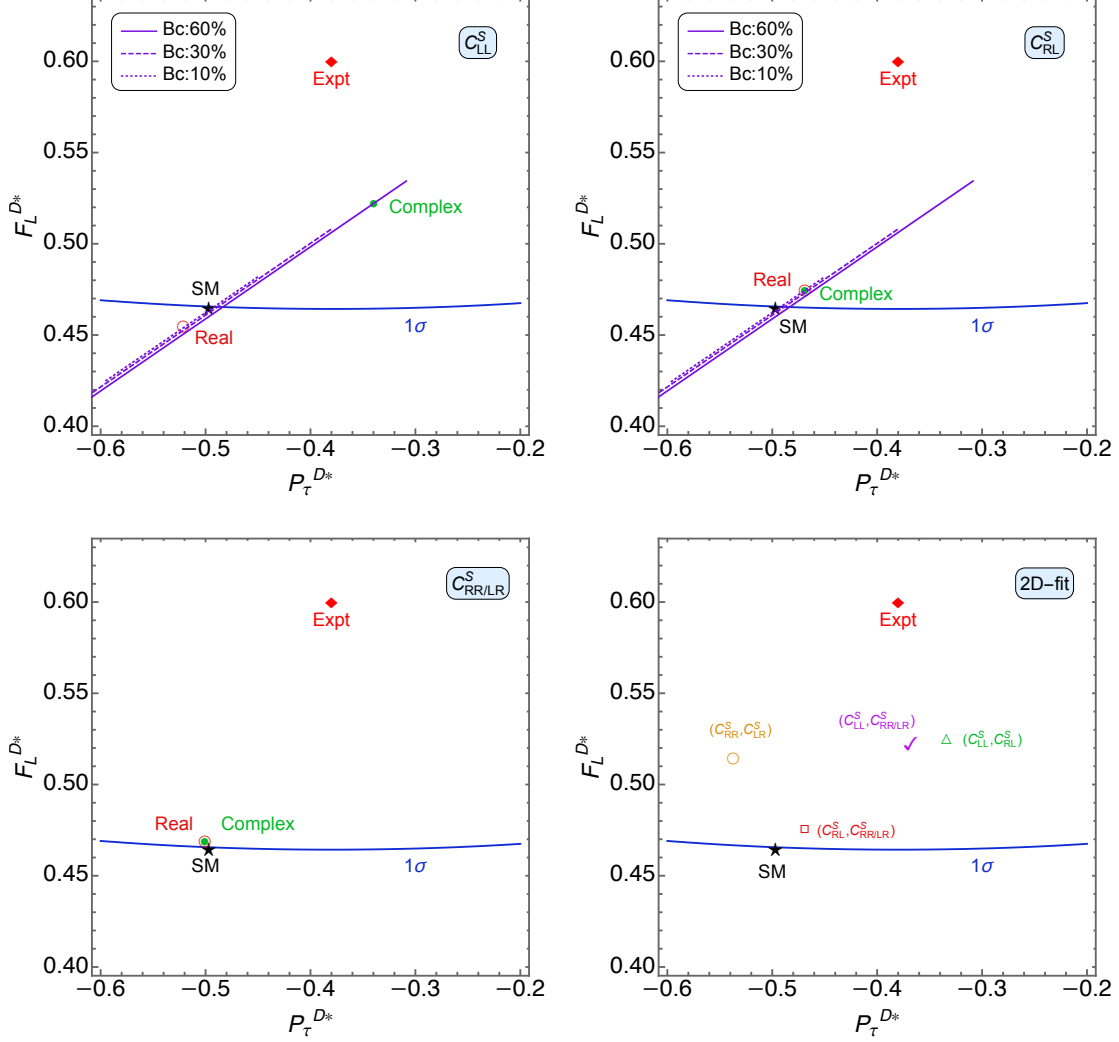


**Figure 2:** Allowed regions with best fit values of scalar couplings in the  $P_\tau^{D^*} - F_L^{D^*}$  plane. The experimental measurement is shown with red diamond, along with the  $1\sigma$  contour in solid blue color. The black star, red circle and green point represent the SM prediction, real and complex fit to the experimental measurement of  $P_\tau^{D^*} - F_L^{D^*}$ , respectively. The purple colored solid, dashed and dotted lines correspond to  $\mathcal{B}(B_c \rightarrow \tau \bar{\nu}) = Bc = 60\%$ ,  $30\%$  and  $10\%$ , respectively.

- In the upper left plot, while considering the real  $C_{LL}^S$  coupling, the fit value of  $P_\tau^{D^*} - F_L^{D^*}$  is observed to lie close to the SM results. However, in the presence of complex  $C_{LL}^S$  coupling, the fit value shifts closer to the experimental results for  $(P_\tau^{D^*}, F_L^{D^*})$ . Furthermore, they are within the upper bound of  $\mathcal{B}(B_c \rightarrow \tau \bar{\nu})$  at 60%.

- In the upper right plot, one can notice that for both the real and complex  $C_{RL}^S$  couplings, the fit results of  $P_\tau^{D^*} - F_L^{D^*}$ , lie slightly above the SM prediction and within  $1\sigma$  contour. In addition, they are within the maximal allowed region of  $\mathcal{B}(B_c \rightarrow \tau \bar{\nu})$ .
- In the lower left plot, for both the real and complex  $(C_{RL}^S, C_{RR}^S/C_{LR}^S)$  couplings, the fit results align with the SM prediction. Hence, it can be concluded that these couplings may not provide an intriguing explanation for the  $P_\tau^{D^*} - F_L^{D^*}$  anomaly.
- In the presence of  $(C_{LL}^S, C_{RL}^S)$ ,  $(C_{RR}^S, C_{LR}^S)$  and  $(C_{LL}^S, C_{RR}^S/C_{LR}^S)$  couplings, the fit value of  $P_\tau^{D^*} - F_L^{D^*}$  shift towards the experimental results. However, for the  $(C_{RL}^S, C_{RR}^S/C_{LR}^S)$  coupling, the fit value exhibits consistent behavior with the predictions of the SM.

We now proceed to discuss the implication of fit results in the  $R_D - R_{\Lambda_c}$  plane. From Fig. 3, we observe the following:

- In presence of the real  $C_{LL}^S$  coupling, the fit value of  $R_D - R_{\Lambda_c}$  falls within the  $1\sigma$  contour of the experimental results. Additionally, it is within the upper bound of  $\mathcal{B}(B_c \rightarrow \tau \bar{\nu}) = 10\%$ . On the other hand, for the complex  $C_{LL}^S$  coupling, the fitted value of  $R_D - R_{\Lambda_c}$  lies slightly above the upper bound of  $\mathcal{B}(B_c \rightarrow \tau \bar{\nu}) = 60\%$ .
- While considering both real and complex  $C_{RL}^S$  couplings, it is notable that the fit values of  $R_D - R_{\Lambda_c}$  coincide with the upper bound of  $\mathcal{B}(B_c \rightarrow \tau \bar{\nu}) = 10\%$ . Additionally, these fit values are found to be closely aligned with the  $1\sigma$  contour.
- The fitted values for  $R_D - R_{\Lambda_c}$  tend to align closely with the  $1\sigma$  uncertainty range in the presence of  $C_{RR}^S/C_{LR}^S$  couplings.
- Even though the fit values of  $R_D - R_{\Lambda_c}$  lie within the  $2\sigma$  experimental contour for all 2D couplings, it is important to note that the presence of  $(C_{RL}^S, C_{RR}^S/C_{LR}^S)$  coupling brings  $(R_D, R_{\Lambda_c})$  remarkably close to the  $1\sigma$  contour.

In Fig 4, we show the effects of all the couplings in  $R_{D^*} - R_{\Lambda_c}$  plane. We observe that,

- In the presence of real  $C_{LL}^S$  coupling, the fit value of  $R_{D^*} - R_{\Lambda_c}$  stands at more than  $2\sigma$  away from the experimental results. However, in presence of the complex  $C_{LL}^S$  coupling, although the fit value of  $R_{D^*} - R_{\Lambda_c}$  falls within the  $2\sigma$  experimental contour, it still does not fall in the allowed region of  $\mathcal{B}(B_c \rightarrow \tau \bar{\nu}) \leq 60\%$ .
- In the presence of both real and complex  $C_{RL}^S$  coupling, the fit values of  $R_{D^*} - R_{\Lambda_c}$  lie inside the  $2\sigma$  contour. Also, it is observed that the fit value lie in the allowed region of  $\mathcal{B}(B_c \rightarrow \tau \bar{\nu}) = 10\%$ .

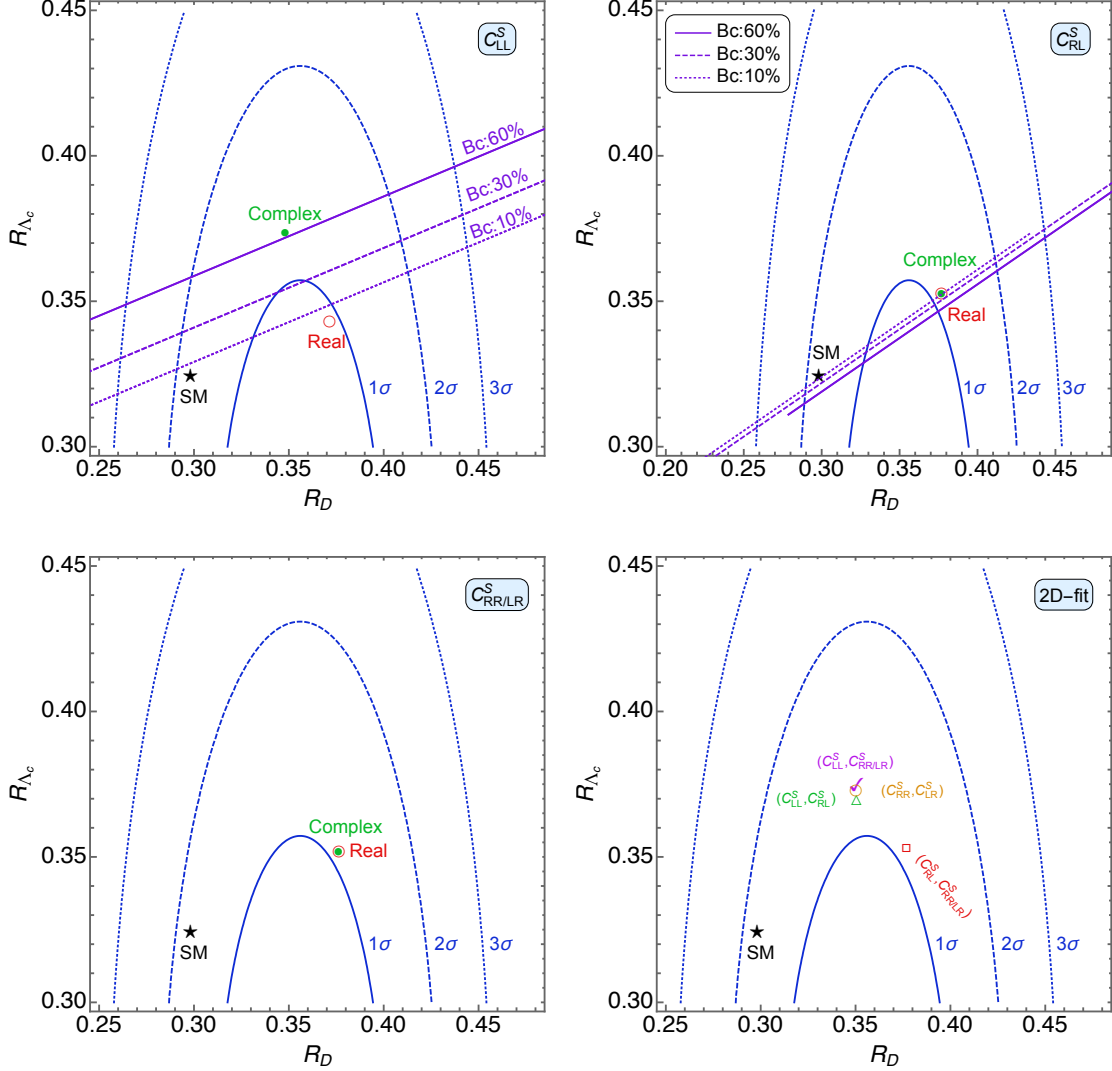


**Figure 3:** Allowed regions with best fit values of scalar couplings in the  $R_D - R_{\Lambda_c}$  plane. The  $1\sigma$ ,  $2\sigma$  and  $3\sigma$  contours are shown in solid, dashed and dotted blue color, respectively. The black star, red circle and green point represent the SM prediction, real and complex fit to the experimental measurement of  $R_D - R_{\Lambda_c}$ , respectively. The purple colored solid, dashed and dotted lines correspond to  $\mathcal{B}(B_c \rightarrow \tau \bar{\nu}) = Bc = 60\%$ ,  $30\%$  and  $10\%$ , respectively.

- In the presence of  $C_{RR}^S/C_{LR}^S$  couplings, the fit value of  $R_{D^*} - R_{\Lambda_c}$  lie within the  $2\sigma$  experimental contour. Similarly in the presence of  $(C_{LL}^S, C_{RL}^S)$ ,  $(C_{RR}^S, C_{LR}^S)$  and  $(C_{LL}^S, C_{RR}^S/C_{LR}^S)$  couplings the fit value lies close to the  $1\sigma$  contour except for the  $(C_{RL}^S, C_{RR}^S/C_{LR}^S)$  which is closer to the  $2\sigma$  contour.

Similarly if we see the Fig. 5, one can observe the following points,

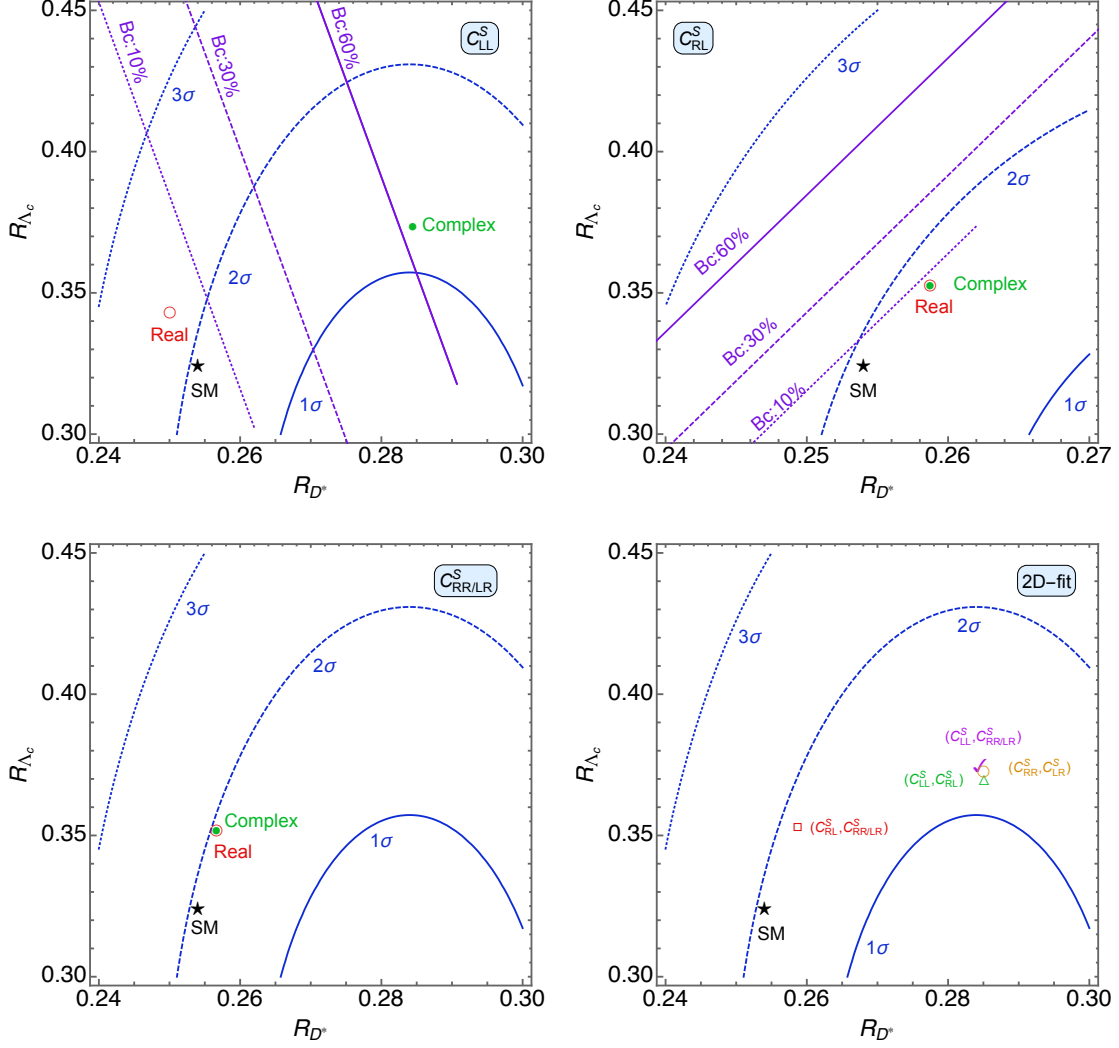


**Figure 4:** Allowed regions with best fit values of scalar couplings in the  $R_{D^*} - R_{\Lambda_c}$  plane. The  $1\sigma$ ,  $2\sigma$  and  $3\sigma$  contours are shown in solid, dashed and dotted blue color, respectively. The black star, red circle and green point represent the SM prediction, real and complex fit to the experimental measurement of  $R_{D^*} - R_{\Lambda_c}$ , respectively. The purple colored solid, dashed and dotted lines correspond to  $\mathcal{B}(B_c \rightarrow \tau \bar{\nu}) = Bc = 60\%$ ,  $30\%$  and  $10\%$ , respectively.

- In the presence of real  $C_{LL}^S$  coupling, the fit results of  $R_D - R_{J/\psi}$  lie within the upper limit of  $\mathcal{B}(B_c \rightarrow \tau \bar{\nu}) = 10\%$ . However the fit value lie above the  $\mathcal{B}(B_c \rightarrow \tau \bar{\nu}) = 60\%$  in the presence of complex  $C_{LL}^S$  coupling.
- In the presence of real and complex  $C_{RL}^S$  coupling, the fit results lie within the allowed region of  $\mathcal{B}(B_c \rightarrow \tau \bar{\nu}) = 10\%$ .

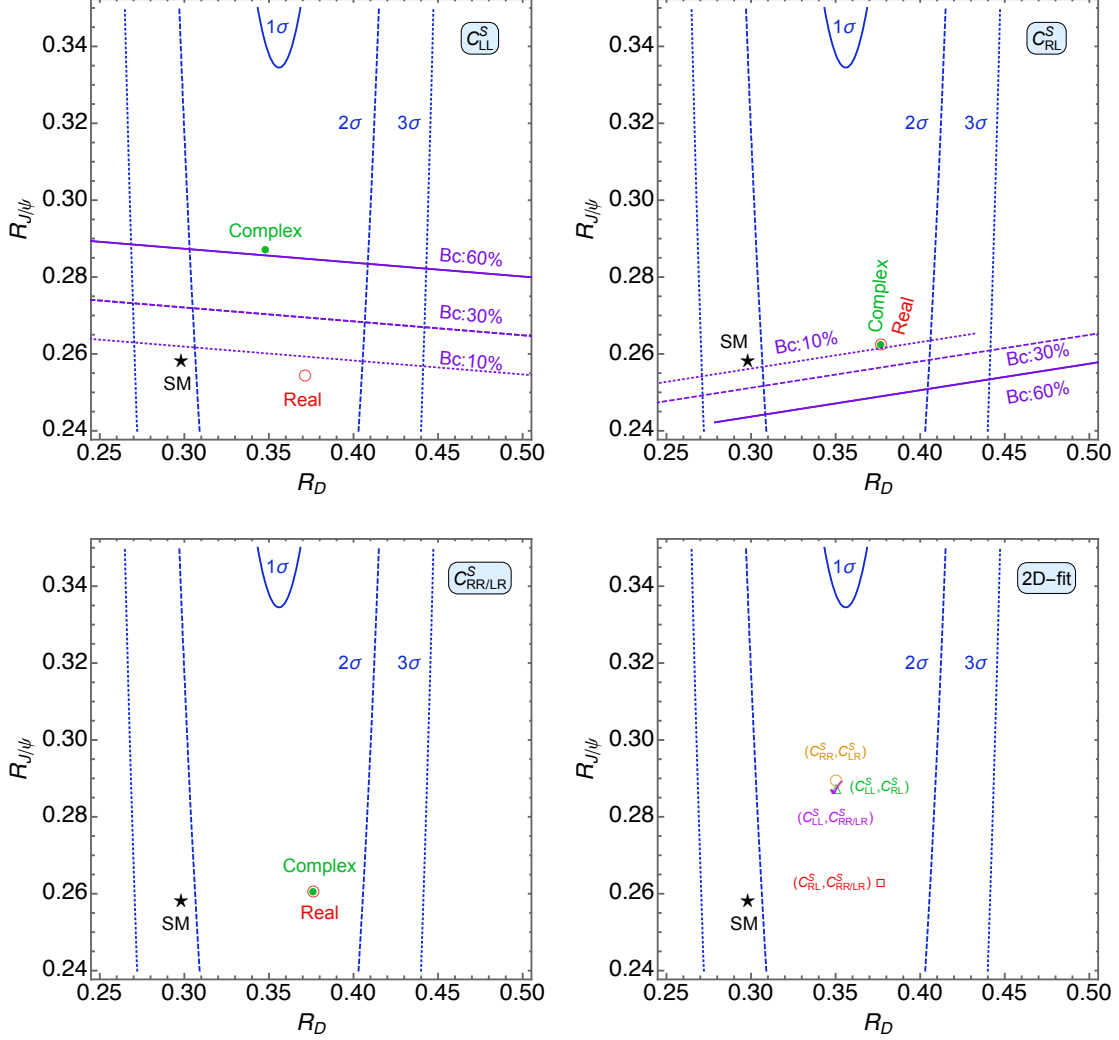


**Figure 5:** Allowed regions with best fit values of scalar couplings in the  $R_D - R_{J/\psi}$  plane. The  $1\sigma$ ,  $2\sigma$  and  $3\sigma$  contours are shown in solid, dashed and dotted blue color, respectively. The black star, red circle and green point represent the SM prediction, real and complex fit to the experimental measurement of  $R_D - R_{J/\psi}$ , respectively. The purple colored solid, dashed and dotted lines correspond to  $\mathcal{B}(B_c \rightarrow \tau \bar{\nu}) = Bc = 60\%$ ,  $30\%$  and  $10\%$ , respectively.

- Similarly for  $C_{RR}^S/C_{LR}^S$  coupling, the fit results lie close to the  $2\sigma$  experimental contour.
- In case of 2D scenario, although the fit values of  $R_D - R_{J/\psi}$  lie within the  $2\sigma$  experimental contour, the fit results for the NP couplings such as  $(C_{RL}^S, C_{RR}^S/C_{LR}^S)$ ,  $(C_{RR}^S, C_{LR}^S)$  and  $(C_{LL}^S, C_{RL}^S)$  fall slightly near to the  $1\sigma$  contour in the  $R_D - R_{J/\psi}$  plane.

Finally, we observe the following from Fig. 6 in the  $R_{D^*} - R_{J/\psi}$  plane:



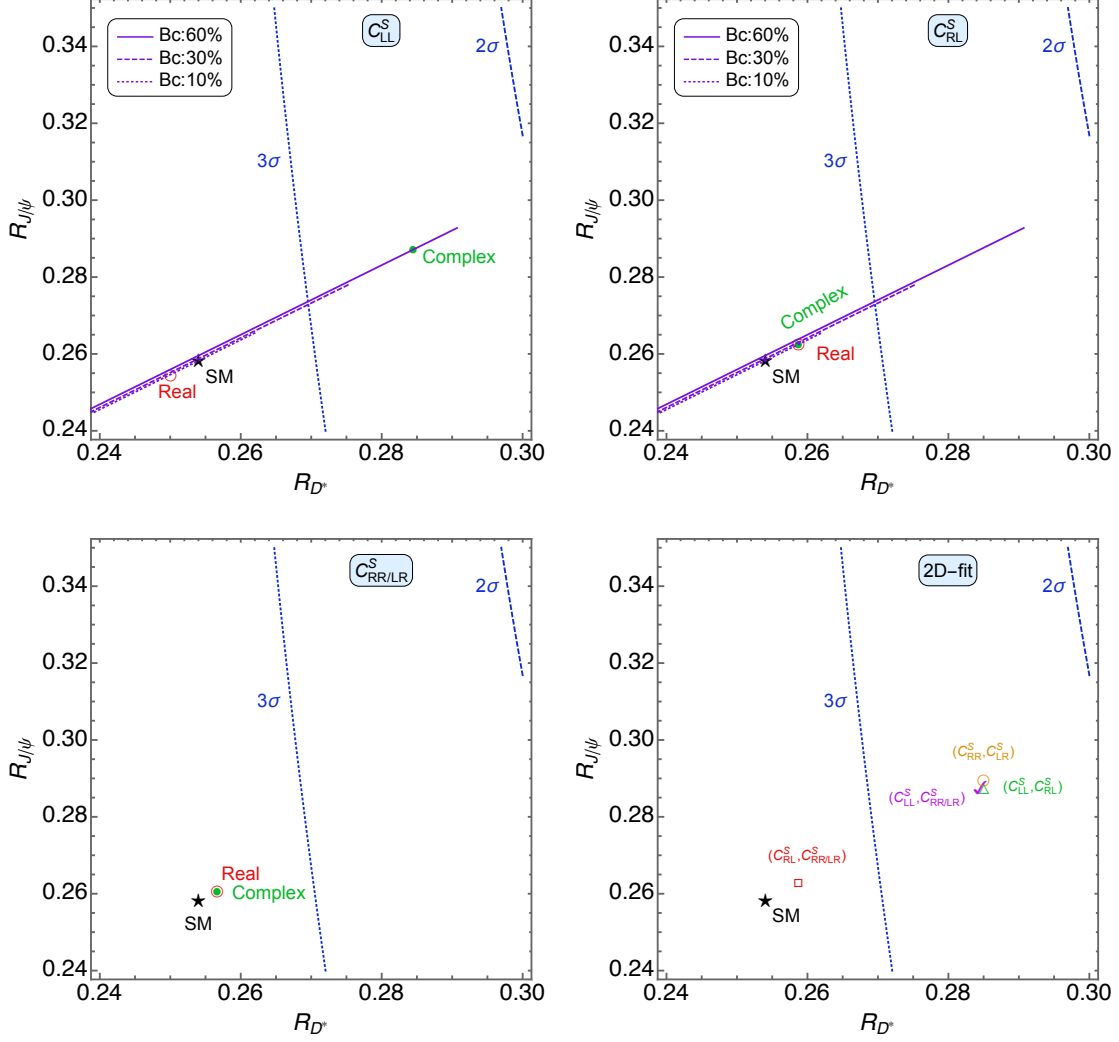


**Figure 6:** Allowed regions with best fit values of scalar couplings in the  $R_{D^*} - R_{J/\psi}$  plane. The  $1\sigma$ ,  $2\sigma$  and  $3\sigma$  contours are shown in solid, dashed and dotted blue color, respectively. The black star, red circle and green point represent the SM prediction, real and complex fit to the experimental measurement of  $R_{D^*} - R_{J/\psi}$ , respectively. The purple colored solid, dashed and dotted lines correspond to  $\mathcal{B}(B_c \rightarrow \tau \bar{\nu}) = B_c = 60\%$ ,  $30\%$  and  $10\%$ , respectively.

- While considering the presence of a real  $C_{LL}^S$  coupling, the observed fit values for  $R_{D^*} - R_{J/\psi}$  fall more than  $3\sigma$  experimental contour. However, in case of a complex  $C_{LL}^S$  coupling, the fit value lie within the  $2\sigma$  experimental contour and also it is not constrained by the branching fraction  $\mathcal{B}(B_c \rightarrow \tau \bar{\nu}) \leq 60\%$ .
- In the presence of both real and complex  $C_{RL}^S$  coupling, the fit values of  $R_{D^*} - R_{J/\psi}$  exceed  $3\sigma$  away from experimental results.

- In the presence of both real and complex  $C_{RR}^S/C_{LR}^S$  coupling, the fit results of  $R_{D^*} - R_{J/\psi}$  lie near the SM prediction and also lie outside the  $3\sigma$  experimental contour.
- The fit value of  $R_{D^*} - R_{J/\psi}$  lie more than  $3\sigma$  away once the  $(C_{RL}^S, C_{RR}^S/C_{LR}^S)$  appear. Interestingly, in the presence of  $(C_{LL}^S, C_{RL}^S)$ ,  $(C_{LL}^S, C_{RR}^S/C_{LR}^S)$ , and  $(C_{RR}^S, C_{LR}^S)$  couplings, it stands within the  $3\sigma$  experimental contour.

As mentioned earlier in section 1, a charged scalar in a generic 2HDM can still explain the combined  $R_D - R_{D^*}$  anomaly. In order to further investigate this possibility, we perform a comprehensive collider analysis to assess the impact of the Large Hadron Collider (LHC) in constraining the  $R_D$ ,  $R_{D^*}$  as well as other anomalies in  $b \rightarrow c\tau\nu$  transition. The details of this collider analysis and its implications will be discussed in the subsequent sections.

## 5 Model description

In our analysis, we examine the charged Higgs boson within the framework of a generic Two Higgs Doublet Model (G2HDM), where both Higgs doublets interact with up-type and down-type quarks. The interaction Lagrangian for the charged Higgs boson ( $H^\pm$ ) in the Higgs basis is expressed as follows [75]:

$$\mathcal{L}_{\text{int}} = y_{bc}^u H^- (\bar{b} P_R c) - y_{bc}^d H^- (\bar{b} P_L c) - y_{\tau\nu} H^- (\bar{\tau} P_L \nu_\tau) + h.c. . \quad (5.1)$$

The Yukawa couplings associated with the up-type and down-type Higgs doublets are denoted as  $y_{bc}^u$  and  $y_{bc}^d$ , respectively. In the general 2HDM, these Yukawa couplings can be complex, which provides the potential for a simultaneous explanation of the  $R_D$  and  $R_{D^*}$  anomalies. However, it should be noted that the Yukawa coupling  $y_{bc}^d$  is constrained by the  $B_s - \bar{B}_s$  mixing [59]. Consequently, the scalar coupling  $C_{RL}^S$  must be very small, leading us to focus on the less constrained coupling  $C_{LL}^S$ . The free parameters of interest in this analysis are  $y_{bc}^u$  (or simply denoted as  $y_{bc}$ ) and  $y_{\tau\nu}$ .

Our focus lies on the  $b \rightarrow c\tau\bar{\nu}$  transition, which is mediated by a charged Higgs boson ( $H^\pm$ ). This transition can be described by an effective Hamiltonian, which can be parameterized as follows:

$$\mathcal{H}_{\text{eff}} = 2\sqrt{2}G_F V_{cb} [(\bar{c}_R \gamma_\mu b_L)(\bar{\tau}_R \gamma^\mu \nu_{\tau L}) + C_{LL}^S (\bar{c}_R b_L)(\bar{\tau}_R \nu_{\tau L})]. \quad (5.2)$$

In this context, the scalar coupling  $C_{LL}^S$  is defined at the scale of the charged Higgs boson mass ( $m_{H^\pm}$ ) as follows:

$$C_{LL}^S = \frac{y_{bc} y_{\tau\nu}}{2\sqrt{2}G_F V_{cb} m_{H^\pm}^2}. \quad (5.3)$$

It is important to note that the value of  $C_{LL}^S$  used in the definition of flavor observables in Eq. 2.3 is defined at the scale of the bottom quark mass ( $m_b$ ). Hence, we employ the renormalization group equation (RGE) running of  $C_{LL}^S$  from the charged Higgs mass scale ( $m_{H^\pm}$ ) to the  $m_b$  scale, following the prescribed procedure outlined in [31].

We do a collider analysis focusing on the final states  $\tau\nu$  and  $b\tau\nu$  in the following sections. These results will subsequently be utilized to impose constraints on the Yukawa couplings under investigation.

## 6 Collider analysis

To address the simultaneous explanation of the  $R_D - R_{D^*}$  anomaly, the collider prospects of a charged Higgs boson in the  $\tau\nu$  final state have been examined in Ref. [75, 76]. It has been demonstrated that the inclusion of an extra b-tagged jet can further enhance the search potential [76]. Previous searches at the LHC have placed constraints on the decay of a charged Higgs boson into a hadronic  $\tau$  ( $\tau_h$ ), primarily through  $W' \rightarrow \tau\nu$  searches [104, 105]. However, these searches still allow for a low-mass range of the charged Higgs boson, with  $m_{H^\pm} \leq 400$  GeV [76].

In this study, we analyze both the  $pp \rightarrow H^\pm \rightarrow \tau_h\nu$  (b-veto category) and  $pp \rightarrow bH^\pm \rightarrow b\tau_h\nu$  (b-tag category) processes, at the HL-LHC. Signal and background events are generated at the leading order (LO) using `MadGraph5_aMC@NLO` [106]. During the event generation process, specific generation-level cuts are applied, and their details can be found in Appendix A (refer to Table 9). Subsequent showering and hadronization of the generated events are carried out using `Pythia8` [107] with the `A14` tune [108] and the `NNPDF2.3NLO` parton distribution function (PDF) set [109]. The reconstruction of jets is performed within the `FastJet` framework [110], utilizing the anti- $k_T$  clustering algorithm [111] with a jet parameter  $R = 0.4$  and a transverse momentum threshold of  $p_T > 15$  GeV. To simulate the detector response, we employ `Delphes-3.5.0` [112] with the default HL-LHC ATLAS analysis card.

The primary source of irreducible background contribution in both the b-veto and b-tag category arises from the  $W \rightarrow \tau\nu$  process (see Fig. 7 (right)). To generate this background, we incorporate two additional jets using the MLM merging scheme [113]. The extra jet can consist of gluon, light quarks,  $c$ -quark, and  $b$ -quark. The next dominant background contamination originates from fake- $\tau_h$  events and Drell-Yan (DY) production. We generate the  $jj\nu\nu$  process, where the light jets, denoted as  $j$ , can mimic a hadronic  $\tau$  ( $\tau_h$ ). We refer

to this background as the "Misid.  $\tau_h$ " background. To improve upon event statistics, we generate the DY process ( $pp \rightarrow \tau\tau$ ) separately in different  $m_{\tau\tau}$  mass regions. These regions are subsequently combined with appropriate cross-section factors. For the di-boson (VV) background, we simulate the  $WW$ ,  $WZ$ , and  $ZZ$  processes separately. The DY+jets and VV+jets backgrounds are generated with two extra jets using the MLM merging scheme [113]. A notable contribution to the background arises from top pair ( $t\bar{t}$ ) production due to its large production cross-section. We generate this background in three categories: fully hadronic  $t\bar{t}$ , semi-leptonic  $t\bar{t}$  (where one  $W$  boson decays hadronically and the other decays leptonically), and fully leptonic  $t\bar{t}$  (where both  $W$  bosons decay leptonically). Lastly, we simulate the single-top background by merging it with one additional jet.

### 6.1 The $\tau_h\nu$ channel

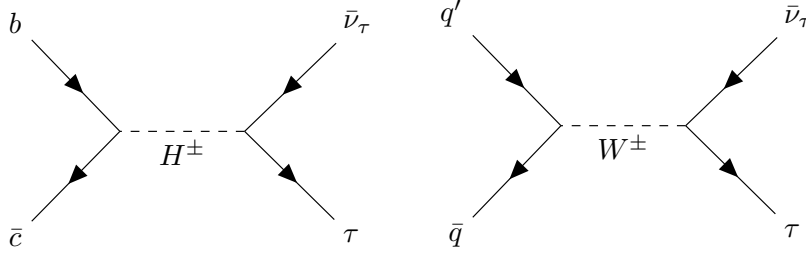


**Figure 7:** *Feynman diagrams for the signal process,  $bc \rightarrow H^\pm \rightarrow \tau\nu$  (left) and the dominant irreducible background,  $pp \rightarrow W^\pm \rightarrow \tau\nu$  (right), at leading order.*

The objective of this section is to investigate the reach of the HL-LHC in constraining low-mass charged Higgs bosons within the general 2HDM model. We perform an optimized cut-based analysis by varying the charged Higgs mass, considering the following benchmark points:  $m_{H^\pm} = 180, 200, 250, 300, 350$  and  $400$  GeV.

Our analysis criteria are as follows: We select events that contain exactly one  $\tau$ -tagged jet with a transverse momentum ( $p_T$ ) greater than 30 GeV and a pseudorapidity ( $|\eta|$ ) within the range of  $|\eta| < 4.0$ . Leptons ( $e, \mu$ ) with  $p_T$  exceeding 20 GeV and  $|\eta|$  within  $|\eta| < 4.0$  are vetoed. Events are required to have zero b-tagged jets with  $p_T$  greater than 30 GeV and  $|\eta|$  within  $|\eta| < 4.0$ . Furthermore, the total number of light jets in an event should not exceed two. This specific requirement significantly reduces the backgrounds from hadronic and semi-leptonic top pair ( $t\bar{t}$ ) production. After applying the generation level cuts used for signal and background generation (see Appendix A), we proceed with a similar analysis as performed by CMS [104] with regards to the basic selection cuts. We impose a cut on the azimuthal angle separation between the  $\tau$ -tagged jet and the missing transverse momentum, requiring  $\Delta\phi(p_{T,\tau_h}, \not{p}_T) \geq 2.4$ . In signal processes, the hadronic  $\tau$  and neutrino are produced nearly

back-to-back. Consequently, the missing transverse momentum and  $p_{T,\tau_h}$  should exhibit small differences, arising from the dilution of neutrino momentum resulting from the  $\tau_h$  decay. Therefore, the ratio of  $p_{T,\tau_h}$  to  $\cancel{p}_T$  is constrained within the range  $0.7 \leq p_{T,\tau_h}/\cancel{p}_T \leq 1.3$ . The normalized kinematic distributions of  $\Delta\phi(p_{T,\tau_h}, \cancel{p}_T)$  and  $p_{T,\tau_h}/\cancel{p}_T$  are presented in Fig. 8 for  $m_{H^\pm} = 180$  and 400 GeV, including all relevant backgrounds.

Cuts applied	
Trigger cuts	Basic selection cuts
$N_{\tau_h} = 1, N_\ell = 0$ b-veto, $N_{\text{b-jets}} = 0$ $N_j \leq 2$	$\Delta\phi(p_{T,\tau_h}, \cancel{p}_T) \geq 2.4$ $0.7 \leq p_{T,\tau_h}/\cancel{p}_T \leq 1.3$
Optimised cuts	
$p_{T,\tau_h} \geq [50, 50, 70, 80, 90, 110] \text{ GeV}$ $m_T \geq [100, 110, 150, 170, 200, 220] \text{ GeV}$ $\cancel{E}_T \geq [50, 50, 60, 80, 90, 100] \text{ GeV}$	for $m_{H^\pm} = [180, 200, 250, 300, 350, 400] \text{ GeV}$

**Table 3:** Cuts imposed on the cut-based analysis in  $pp \rightarrow H^\pm \rightarrow \tau_h \nu$  channel.

Following the selection cuts, we perform a cut-based analysis by optimizing the cuts on three observables: transverse momentum of the  $\tau$ -tagged jet ( $p_{T,\tau_h}$ ), transverse mass ( $m_T$ ), and missing transverse energy ( $\cancel{E}_T$ ). The objective is to maximize the signal significance, defined as  $\sigma_s = S/\sqrt{B}$ , where  $S$  and  $B$  represent the signal and background yields at a given integrated luminosity. Table 3 summarizes the trigger, basic selection, and optimized cuts for each observable. It is observed that the optimized cuts become stricter as the charged Higgs mass increases. This is consistent with the trend observed in Fig. 8, where the signal kinematic distributions become flatter with increasing  $m_{H^\pm}$ , and a stronger cut enhances the separation between the signal and background. To quantify the impact of each cuts, we provide a cut-flow table in Table 4 for  $m_{H^\pm} = 180$  and 400 GeV. This table illustrates the number of background events at the HL-LHC and signal efficiency remaining after each stage of the analysis, allowing for a clear understanding of the signal and background contributions at each step.

As previously mentioned, the  $N_j \leq 2$  cut effectively reduces the  $t\bar{t}$  background, resulting in a significant suppression. The  $\Delta\phi(p_{T,\tau_h}, \cancel{p}_T)$  cut plays a crucial role in reducing all backgrounds while minimally affecting the signal process. For  $m_{H^\pm} = 400$  GeV, the optimized cuts on  $p_{T,\tau_h}$ ,  $m_T$ , and  $\cancel{E}_T$  lead to a reduction in all backgrounds by approximately one to two orders of magnitude. In Table 5, we provide the background yields and signal efficiencies after the cut-based analysis for  $m_{H^\pm} = 200, 250, 300$ , and 350 GeV. Indeed, for lower values of  $m_{H^\pm} = 180$  GeV, the W+jets background contamination is significant, accounting for

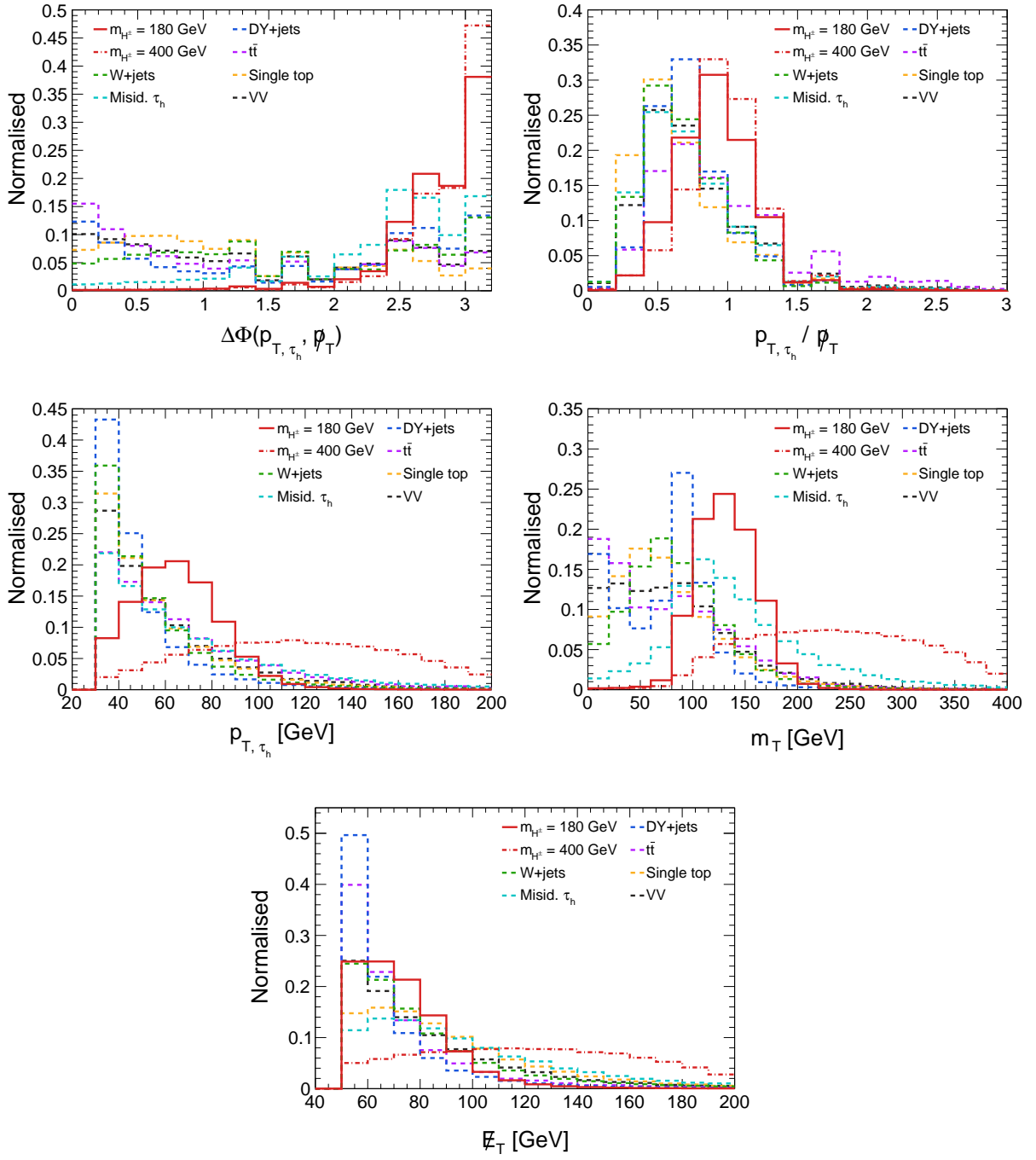


**Figure 8:** The normalised kinematic distributions of  $\Delta\phi(p_{T,\tau_h}, p_T)$ ,  $p_{T,\tau_h}/p_T$ ,  $p_{T,\tau_h}$ ,  $m_T$  and  $\cancel{E}_T$  for charged Higgs masses of  $m_{H^\pm} = 180$  and  $400$  GeV with backgrounds, for the  $b$ -veto category. The distributions are shown after the basic trigger and generation level cuts.

Cut flow	Signal	Background rates at $\sqrt{s} = 14$ TeV with $\mathcal{L} = 3 \text{ ab}^{-1}$							
	Efficiency, $\epsilon$ ( $\times 10^{-2}$ )	W+jets	Misid. $\tau_h$	DY+jets	$t\bar{t}$ had	$t\bar{t}$ semi-lep	$t\bar{t}$ lep	VV+jets	Single $t$
		$(\times 10^7)$			$(\times 10^5)$			$(\times 10^6)$	
$m_{H^\pm} = 180 \text{ GeV}$									
Trigger+Gen	19.9	14.9	2.0	4.3	10.1	44.5	7.8	9.7	3.1
$N_j \leq 2$	19.8	13.6	1.7	3.9	2.0	22.4	6.3	7.2	2.4
$\Delta\phi(p_{T,\tau_h}, \cancel{p}_T)$	17.8	4.7	1.1	1.7	0.6	3.2	2.2	2.1	0.5
$p_{T,\tau_h}/\cancel{p}_T$	13.0	2.8	0.44	0.86	0.25	1.3	0.8	0.9	0.2
$p_{T,\tau_h}$	11.5	2.2	0.41	0.43	0.20	1.1	0.75	0.77	0.16
$m_T$	10.7	2.1	0.41	0.40	0.19	1.1	0.72	0.75	0.16
$\cancel{E}_T$	10.7	2.1	0.41	0.40	0.19	1.1	0.72	0.75	0.16
$m_{H^\pm} = 400 \text{ GeV}$									
Trigger+Gen	28.0	14.9	2.0	4.3	10.1	44.5	7.8	9.7	3.1
$N_j \leq 2$	27.7	13.6	1.7	3.9	2.0	22.4	6.3	7.2	2.4
$\Delta\phi(p_{T,\tau_h}, \cancel{p}_T)$	25.5	4.7	1.1	1.7	0.6	3.2	2.2	2.1	0.5
$p_{T,\tau_h}/\cancel{p}_T$	20.0	2.8	0.44	0.86	0.25	1.3	0.8	0.9	0.2
$p_{T,\tau_h}$	12.4	0.14	0.12	0.02	0.01	0.2	0.14	0.12	0.03
$m_T$	11.0	0.12	0.11	0.01	0.008	0.18	0.12	0.11	0.02
$\cancel{E}_T$	11.0	0.12	0.11	0.01	0.008	0.18	0.12	0.11	0.02

**Table 4:** Signal efficiency and background yields at the HL-LHC, in the  $pp \rightarrow H^\pm \rightarrow \tau_h \nu$  channel, at each step of the cut-based analysis for the charged Higgs mass of  $m_{H^\pm} = 180$  and 400 GeV.

approximately 70% of the total background yield. The Misid.  $\tau_h$  and DY+jets backgrounds contribute approximately 13% each. However, as  $m_{H^\pm}$  increases, the signal and backgrounds become better separated, as evident from the kinematic distributions of  $p_{T,\tau_h}$ ,  $m_T$ , and  $\cancel{E}_T$  in Fig. 8. This leads to a reduction in the W+jets background yield, and the contribution from Misid. $\tau_h$  becomes closer to the dominant W+jets background. For instance, after the cut-based analysis, the W+jets and Misid.  $\tau_h$  backgrounds contribute approximately 47% and 42% to the total background yield, respectively, for  $m_{H^\pm} = 400 \text{ GeV}$ .

To calculate the projected upper limit on the charged Higgs production cross-section in a model-independent way, we use the following formula:

$$\sigma(pp \rightarrow H^\pm \rightarrow \tau_h \nu)_{\text{UL}} = \frac{N \cdot \sqrt{B}}{\epsilon \cdot \mathcal{L}} \quad (6.1)$$

where:

$pp \rightarrow H^\pm \rightarrow \tau_h \nu, \sqrt{s} = 14 \text{ TeV}$									
Masses	Background yields after the cut-based analysis at $3 \text{ ab}^{-1}$								Signal Efficiency,
$m_{H^\pm}$	W+jets	Misid. $\tau_h$	DY+jets	$t\bar{t}$ had	$t\bar{t}$ semi-lep	$t\bar{t}$ lep	VV+jets	Single $t$	$\epsilon$
(GeV)	$(\times 10^7)$			$(\times 10^5)$			$(\times 10^6)$		$(\times 10^{-2})$
200	1.9	0.4	0.3	0.2	1.1	0.7	0.7	0.15	11.6
250	0.6	0.3	0.06	0.05	0.6	0.4	0.35	0.08	$\sim 10$
300	0.36	0.2	0.04	0.03	0.4	0.3	0.25	0.06	10.9
350	0.2	0.16	0.02	0.02	0.3	0.2	0.16	0.04	10.9

**Table 5:** Signal efficiency and background yields after the cut-based analysis in the  $pp \rightarrow H^\pm \rightarrow \tau_h \nu$  channel at the HL-LHC.

- $\sigma(pp \rightarrow H^\pm \rightarrow \tau_h \nu)_{\text{UL}}$  is the projected upper limit on the charged Higgs production cross-section in the  $\tau_h \nu$  final state.
- $N$  is the number of confidence intervals or the desired significance level. For example, a 95% confidence level corresponds to  $N = 2$ .
- $B$  is the total background yield, which is the sum of all background events after the cut-based analysis.
- $\epsilon$  is the signal efficiency, representing the fraction of signal events that pass the selection cuts.
- $\mathcal{L}$  is the integrated luminosity, which denotes the total amount of data collected.

By plugging in the appropriate values for  $N$ ,  $B$ ,  $\epsilon$ , and  $\mathcal{L}$  from our analysis, we calculate the projected upper limit on the charged Higgs production cross-section. This provides an estimate of the maximum allowed cross-section for the charged Higgs production in the  $\tau_h \nu$  final state based on the analysis results and the chosen confidence level.

We evaluate the  $\sigma(pp \rightarrow H^\pm \rightarrow \tau_h \nu)_{\text{UL}}$  at different confidence levels, such as 95% (exclusion limit) and 99.7% (discovery limit), corresponding to  $2\sigma$  and  $5\sigma$  significance levels, respectively. The derived upper limits are shown as solid green and purple lines in Fig. 9. For example, for the  $2\sigma$  upper limit, the values vary in the range  $[32.26 : 7.38] \text{ fb}$  for  $m_{H^\pm} = [180 : 400] \text{ GeV}$ . These values represent the maximum allowed cross-section for the charged Higgs production in the  $\tau_h \nu$  final state at a 95% confidence level. In addition, a systematic uncertainty of 2% is included in the analysis. The resulting upper limits, accounting for this systematic uncertainty, are shown as dashed colored lines in Fig. 9. It is worth noting that the presence of systematics can weaken the limits due to the significant contamination from



the  $W$ +jets background, which constitutes a substantial fraction of the total background (approximately 50 – 70%) in this channel.

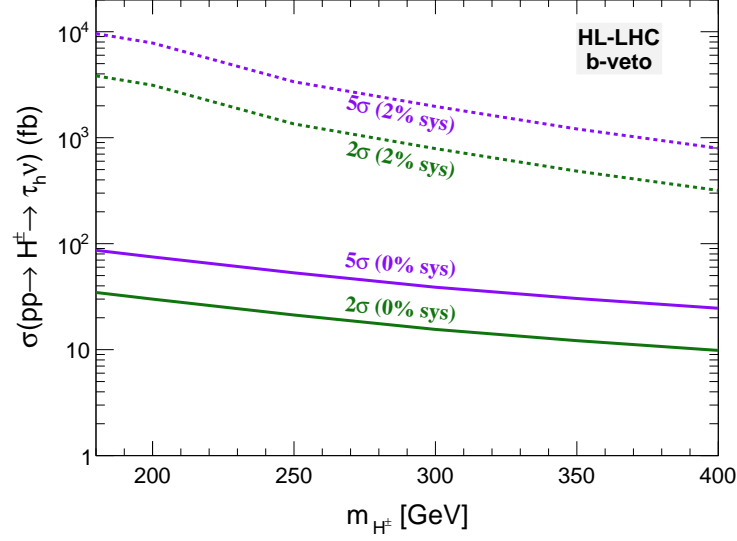


**Figure 9:** Upper limit on  $\sigma(pp \rightarrow H^\pm \rightarrow \tau\nu)$  as a function of  $m_{H^\pm}$  in the  $b$ -veto category. The green and purple solid (dashed) lines show the  $2\sigma$  and  $5\sigma$  upper limit upon including 0% (2%) systematic uncertainties.

## 6.2 The $b\tau_h\nu$ channel

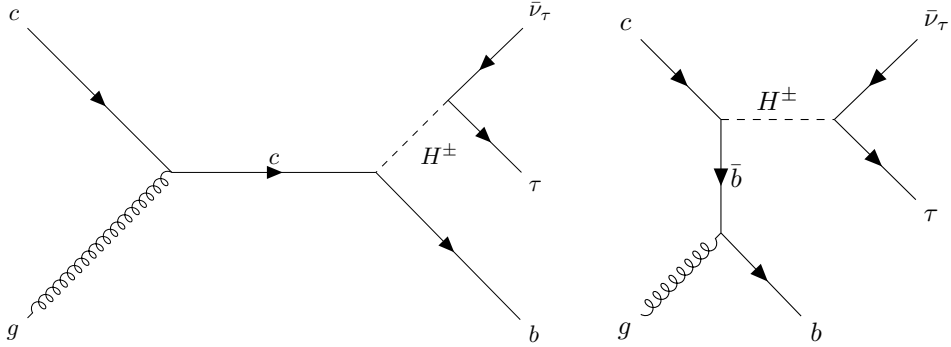


**Figure 10:** The Feynman diagrams for the signal process  $gc \rightarrow bH^\pm \rightarrow b\tau\nu$  in the  $b$ -tag category at leading order.

In the  $pp \rightarrow bH^\pm \rightarrow b\tau\nu$  channel, the charged Higgs boson is produced in association with a bottom quark. This final state is characterized by the presence of one  $b$ -tagged jet, along with the hadronically decaying tau lepton ( $\tau_h$ ) and missing transverse energy ( $\cancel{E}_T$ ).

The leading order Feynman diagrams for the signal process are shown in Fig. 10. We select events with exactly one  $\tau$ -tagged jet with  $p_T > 30$  GeV and  $|\eta| < 4.0$ . Leptons are vetoed having  $p_T > 20$  GeV and  $|\eta| < 4.0$ . Events are required to have exactly one b-tagged jet with  $p_T > 30$  GeV and  $|\eta| < 4.0$ . We further restrict the total number of light jets to be at most two.

The normalised kinematic distributions of  $\Delta\phi(p_{T,\tau_h}, \not{p}_T)$ ,  $p_{T,\tau_h}/\not{p}_T$ ,  $p_{T,\tau_h}$ ,  $m_T$ , and  $\cancel{E}_T$  for the  $pp \rightarrow bH^\pm \rightarrow b\tau\nu$  channel are shown in Fig. 11. From the distributions, we observe that the signal and backgrounds overlap for the  $p_{T,\tau_h}/\not{p}_T$  distribution. This can be understood by considering the additional b-jet present in the signal process. The charged Higgs recoils against the b-jet, which further decays to  $\tau\nu$ . The momentum imbalance of the b-jet and the hadronically decaying  $\tau$  lepton contributes to the total missing transverse energy ( $\cancel{E}_T$ ) in the event. As a result, the overall  $\cancel{E}_T$  is higher compared to the previous b-veto signal category. The transverse momentum of the  $\tau$  lepton is slightly lower in this final state. These factors lead to a decrease in the ratio  $p_{T,\tau_h}/\not{p}_T$ , causing the signal distribution to overlap with the background processes. Therefore, we exclude this observable from further optimization. Instead, we focus on four kinematic observables for the cut-based optimization:  $\Delta\phi(p_{T,\tau_h}, \not{p}_T)$ ,  $p_{T,\tau_h}$ ,  $m_T$ , and  $\cancel{E}_T$ . These observables exhibit better discrimination between the signal and background processes. The trigger-level cuts and the optimized cuts for these observables are summarized in Table 6. These cuts are chosen to enhance the signal significance and improve the sensitivity of the analysis.

Cuts applied	
Trigger cuts	
$N_{\tau_h} = 1, N_\ell = 0$ b-tag, $N_{\text{b-jets}} = 1$ $N_j \leq 2$	
Optimised cuts	
$p_{T,\tau_h} \geq [30, 30, 40, 50, 50, 60]$ GeV $\Delta\phi(p_{T,\tau_h}, \not{p}_T) \geq [1.1, 1.0, 0.9, 0.7, 1.0, 1.0]$ $m_T \geq [100, 110, 140, 170, 200, 230]$ GeV $\cancel{E}_T \geq [50, 50, 60, 70, 80, 100]$ GeV	for $m_{H^\pm} = [180, 200, 250, 300, 350, 400]$ GeV

**Table 6:** Trigger-level and optimised cuts imposed on the cut-based analysis in b-tag category.

The signal efficiency and background yields after each optimized cut for the  $pp \rightarrow bH^\pm \rightarrow b\tau\nu$  channel at an integrated luminosity of  $3 \text{ ab}^{-1}$  are presented in Table 7. The most effective observable in reducing the backgrounds is the transverse mass,  $m_T$ . The cut on  $m_T$

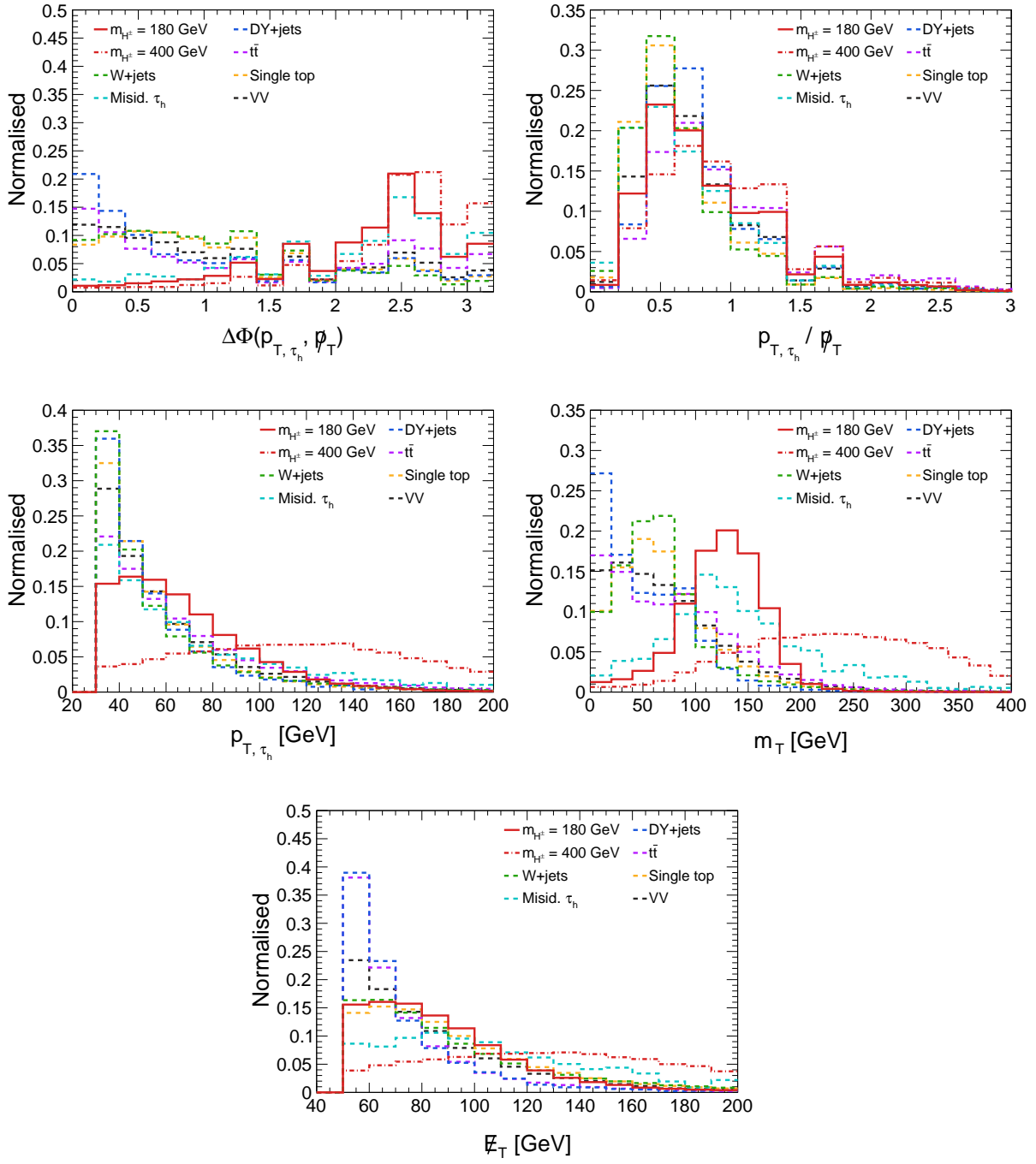


**Figure 11:** The normalised kinematic distributions of  $\Delta\phi(p_{T,\tau_h}, p_T)$ ,  $p_{T,\tau_h}/p_T$ ,  $p_{T,\tau_h}$ ,  $m_T$  and  $\cancel{E}_T$  for charged Higgs masses of  $m_{H^\pm} = 180$  and  $400$  GeV with backgrounds, for the  $b$ -tag category. The distributions are shown after the basic trigger and generation level cuts.

becomes stronger as the charged Higgs mass increases, resulting in a reduction of the dominant W+jets background by approximately one order of magnitude. The  $\Delta\phi(p_{T,\tau_h}, \cancel{p}_T)$  variable is also effective in suppressing all background processes with a negligible impact on the signal efficiency. It helps to enhance the signal-to-background ratio by exploiting the back-to-back nature of the signal process, where the hadronically decaying  $\tau$  and the missing transverse momentum are almost in opposite directions with dilution coming from the additional b-jet in this b-tag category. In Table 8, we provide the signal efficiency and background yields at a center-of-mass energy of  $\sqrt{s} = 14$  TeV for charged Higgs mass,  $m_{H^\pm} = 200, 250, 300$ , and 350 GeV. These results demonstrate the effectiveness of the optimized cuts in enhancing the signal significance and reducing the background contributions.

Cut flow	Signal	Background rates at $\sqrt{s} = 14$ TeV with $\mathcal{L} = 3 \text{ ab}^{-1}$							
	Efficiency, $\epsilon$ ( $\times 10^{-2}$ )	W+jets	Misid. $\tau_h$	DY+jets	$t\bar{t}$ had	$t\bar{t}$ semi-lep	$t\bar{t}$ lep	VV+jets	Single $t$
		( $\times 10^6$ )			( $\times 10^5$ )			( $\times 10^6$ )	
$m_{H^\pm} = 180 \text{ GeV}$									
Trigger+Gen	7.0	4.8	0.6	1.8	18.3	83.5	15.6	8.0	5.2
$N_j \leq 2$	6.9	4.4	0.5	1.6	5.3	52.9	13.7	7.2	4.6
$p_{T,\tau_h}$	6.9	4.4	0.5	1.6	5.3	52.9	13.7	7.2	4.6
$\Delta\phi(p_{T,\tau_h}, \cancel{p}_T)$	6.3	2.0	0.44	0.6	3.0	21.5	9.7	3.5	2.2
$m_T$	4.8	0.6	0.36	0.2	1.8	9.4	6.0	1.8	1.0
$\cancel{E}_T$	4.8	0.6	0.36	0.2	1.8	9.4	6.0	1.8	1.0
$m_{H^\pm} = 400 \text{ GeV}$									
Trigger+Gen	13.0	4.8	0.6	1.8	18.3	83.5	15.6	8.0	5.2
$N_j \leq 2$	12.3	4.4	0.5	1.6	5.3	52.9	13.7	7.2	4.6
$p_{T,\tau_h}$	10.8	1.3	0.3	0.5	2.7	18.0	4.5	2.6	1.5
$\Delta\phi(p_{T,\tau_h}, \cancel{p}_T)$	10.4	0.5	0.2	0.2	1.6	7.6	3.5	1.3	0.7
$m_T$	5.8	0.06	0.07	0.006	0.2	0.7	0.43	0.1	0.06
$\cancel{E}_T$	5.5	0.05	0.07	0.003	0.07	0.6	0.4	0.1	0.06

**Table 7:** Signal efficiency and background yields at the HL-LHC, in the  $pp \rightarrow bH^\pm \rightarrow b\tau_h\nu$  channel, at each step of the cut-based analysis for the charged Higgs mass of  $m_{H^\pm} = 180$  and 400 GeV.

Finally, we investigate the upper limits on the production cross-section, denoted as  $\sigma(pp \rightarrow bH^\pm \rightarrow b\tau_h\nu)_{UL}$ , in relation to the charged Higgs mass. The corresponding results are illustrated in Fig. 12. For the charged Higgs mass range of  $180 \text{ GeV} \leq m_{H^\pm} \leq 400 \text{ GeV}$ , the 95% confidence level (CL) upper limit, without any systematic uncertainties, exhibits a variation from 31.89 fb to 6.84 fb. When considering a 2% systematic uncertainty, the  $2\sigma$  upper limit is approximately 70.26 fb for  $m_{H^\pm} = 400 \text{ GeV}$ . Despite the additional

$pp \rightarrow bH^\pm \rightarrow b\tau_h\nu, \sqrt{s} = 14 \text{ TeV}$									
Masses	Background yields after the cut-based analysis at $3 \text{ ab}^{-1}$								Signal Efficiency,
$m_{H^\pm}$	W+jets	Misid. $\tau_h$	DY+jets	$t\bar{t}$ had	$t\bar{t}$ semi-lep	$t\bar{t}$ lep	VV+jets	Single $t$	$\epsilon$
(GeV)	$(\times 10^6)$			$(\times 10^5)$			$(\times 10^6)$		$(\times 10^{-2})$
200	0.5	0.3	0.15	1.5	7.7	5.0	1.5	0.8	5.3
250	0.3	0.2	0.05	0.6	3.9	2.5	0.7	0.4	5.4
300	0.14	0.15	0.02	0.3	2.0	1.3	0.4	0.2	5.5
350	0.08	0.1	0.009	0.16	1.1	0.7	0.2	0.1	5.6

**Table 8:** Signal efficiency and background yields after the cut-based analysis in the  $pp \rightarrow bH^\pm \rightarrow b\tau_h\nu$  channel at the HL-LHC.

b-tagging requirement favoring the  $t\bar{t}$  background, this condition significantly suppresses the dominant W+jets background. Consequently, the upper limit in this channel becomes more stringent compared to the previously discussed  $pp \rightarrow H^\pm \rightarrow \tau\nu$  final state due to a higher signal-to-background ratio (S/B).

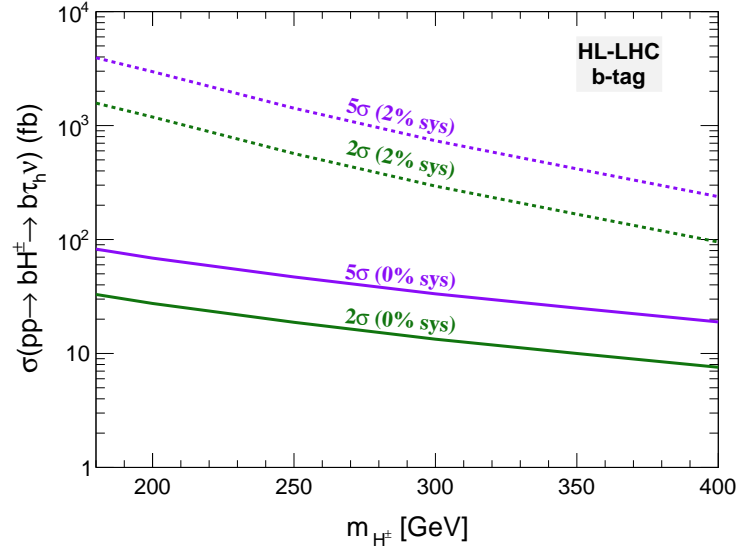


**Figure 12:** Upper limit on  $\sigma(pp \rightarrow H^\pm \rightarrow \tau\nu)$  as a function of charged Higgs mass in the  $b$ -tag category. The green and purple solid (dashed) lines show the  $2\sigma$  and  $5\sigma$  upper limit upon including 0% (2%) systematic uncertainties.

## 7 Collider prospect of flavor anomalies

In the present section, we analyse the ramifications arising from the implementation of upper limits on the cross-section of charged Higgs production, focusing on their impact on the Yukawa parameter space as well as the extent to which the HL-LHC can effectively probe the diverse anomalies observed in the  $b \rightarrow c\tau\nu$  decay processes.

### 7.1 Constraining the Yukawa couplings

In section 5, we have extensively examined the scalar coupling  $C_{LL}^S$ , which is directly proportional to the product of the charged Higgs Yukawa couplings,  $y_{bc} \times y_{\tau\nu}$ . Expanding on the findings of our collider analysis presented in the preceding section (section 6), the primary objective of this section is to impose constraints on the two-dimensional parameter space of Yukawa couplings, namely  $|y_{bc}| - |y_{\tau\nu}|$ . Throughout this investigation, the charged Higgs mass is considered to lie within the range of  $[180, 400]$  GeV. In section 4.1, we have discussed several observables, namely  $R_D$ ,  $R_D^*$ ,  $P_\tau^{D^*}$ ,  $F_L^{D^*}$ ,  $R_{J/\psi}$ , and  $R_{\Lambda_c}$ , which exhibit sensitivity to the phase of the Yukawa couplings. To determine the phase, we perform a fit by minimizing a  $\chi^2$  value constructed from these flavor observables. Once the phase is determined, we present the  $1\sigma$ ,  $2\sigma$  and  $3\sigma$  region, represented by the darker yellow, light yellow and green band in Fig. 13, which demonstrates consistency with current measurements of all the considered flavor observables.

To further constrain the parameter space, the large  $y_{bc}$  values are subject to limitations imposed by the  $B_s - \bar{B}_s$  mixing, as illustrated by the gray colored region in the figure. In this constraint calculation, we account for the renormalization group equation (RGE) running effect of the strong coupling constant  $\alpha_s$  [114]. The contribution of the charged Higgs to the  $B_s - \bar{B}_s$  mixing, occurring at the 1-loop level, is taken from [68], and we follow [115] to impose constraint on this parameter. Additionally, the region below the blue solid, dashed, and dotted colored lines in Fig. 13 corresponds to the allowed parameter space considering a branching ratio of approximately 60%, 30%, and 10% for  $\mathcal{B}(B_c \rightarrow \tau\nu)$ , respectively.

Finally, we incorporate the 95% confidence level (CL) upper limits obtained from the  $\tau_h\nu$  (b-veto category) and  $b\tau_h\nu$  (b-tag category) searches discussed in the previous section. These upper limits are represented by the green and purple colored lines, respectively, in Fig. 13 on the  $|y_{bc}| - |y_{\tau\nu}|$  parameter space.

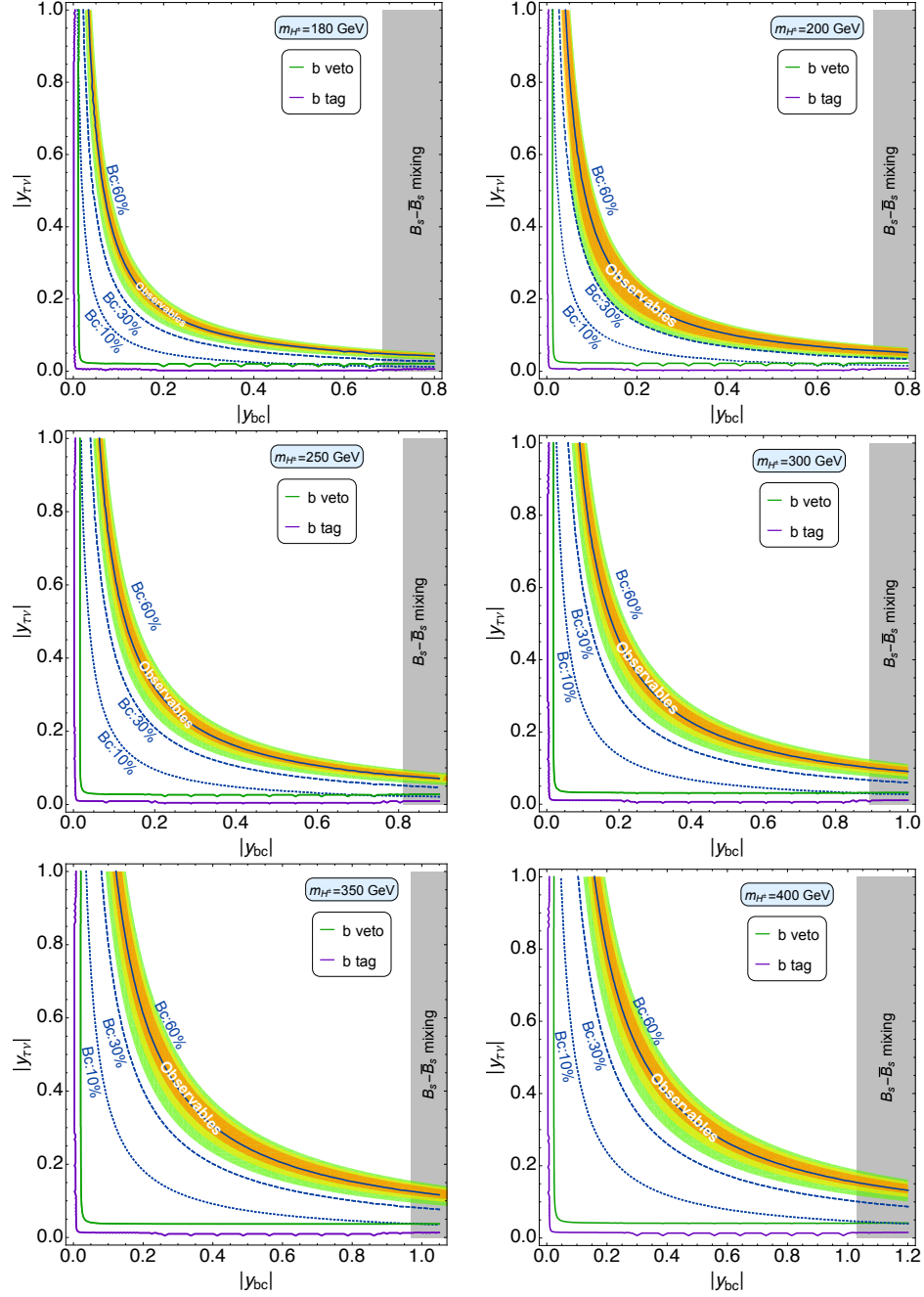


**Figure 13:** Constraints on  $|y_{bc}| - |y_{\tau\nu}|$  parameter space for various charged Higgs masses. The darker yellow, light yellow and green bands indicate the  $1\sigma$ ,  $2\sigma$  and  $3\sigma$  region in consonant with the current measurement of corresponding flavor observables. Here,  $B_c$  represents the  $\mathcal{B}(B_c \rightarrow \tau\nu)$ . The collider constraints are shown with green and purple lines for  $b$ -veto and  $b$ -tag analysis, respectively.

## 7.2 Constraining the flavor observables

Finally, we present the study of the HL-LHC reach in the  $\tau\nu$  and  $b\tau\nu$  final states, aiming to provide an explanation for the observed anomalies in  $b \rightarrow c\tau\nu$  decays. The results are illustrated in Figure 14. As mentioned earlier in Section 4.3, we display the  $1\sigma$ ,  $2\sigma$ , and  $3\sigma$  contours representing the world averages of flavor observables in solid, dashed, and dotted blue lines, respectively. The purple solid, dashed, and dotted lines correspond to the branching ratios  $\mathcal{B}(B_c \rightarrow \tau\nu)$  of 60%, 30% and 10%, respectively. The black star denotes the SM prediction. Notably, the grey shaded region lies outside the accessible range within the current model.

Furthermore, we select two benchmark points based on the collider constraints obtained in the  $|y_{bc}| - |y_{\tau\nu}|$  plane. Specifically, we consider the points  $(|y_{bc}|, |y_{\tau\nu}|) \sim (0.6, 0.0065)$  and  $(0.9, 0.0155)$  for the b-veto and b-tag categories, respectively. These constraints are then translated into the 2D plane of flavor observables, as shown in Figure 14. In the figure, we represent the benchmark points for the b-veto and b-tag categories with a green-colored point and a tick symbol, respectively, considering  $m_{H^\pm} = 180$  GeV. Similarly, we use brown-colored symbols to denote the benchmark points for  $m_{H^\pm} = 400$  GeV.

In the  $R_D - R_{D^*}$  plane, both the b-veto and b-tag analyses exhibit sensitivity up to the  $3\sigma$  region across the considered mass range for the charged Higgs boson. However, it is important to note that there is a significant experimental uncertainty associated with the measurements of  $P_\tau^{D^*}$  and  $F_L^{D^*}$ . In the current model, only a small portion of the  $1\sigma$  and  $2\sigma$  regions can be covered. Moving to the  $R_D - R_{\Lambda_c}$  plane, the  $\tau\nu$  final state demonstrates sensitivity up to the  $2\sigma$  region for  $m_{H^\pm} = 180$  GeV, and up to the  $3\sigma$  region for  $m_{H^\pm} = 400$  GeV. On the other hand, the  $b\tau\nu$  channel exhibits sensitivity to the  $3\sigma$  region for both masses of the charged Higgs. It should be noted that variations in the complex phase of the Yukawa couplings have an impact on the prediction of  $R_{D^*}$ , and the collider limits derived from the b-veto and b-tag categories show sensitivity up to the  $2\sigma$  region in the  $R_{D^*} - R_{\Lambda_c}$  plane. Regarding the  $R_D - R_{J/\psi}$  plane, the  $1\sigma$  region lies outside the prediction range of the current model. However, a significant portion of the  $2\sigma$  and  $3\sigma$  regions falls within the reach of the  $\tau\nu$  final state, while the  $b\tau\nu$  channel demonstrates sensitivity up to the  $3\sigma$  region within the model prediction region. In the  $R_{D^*} - R_{J/\psi}$  plane, the model prediction covers a relatively narrow range, but the sensitivity extends to the  $3\sigma$  region. This can be correlated to the large uncertainty associated with the experimental measurement of the  $R_{J/\psi}$  observable.



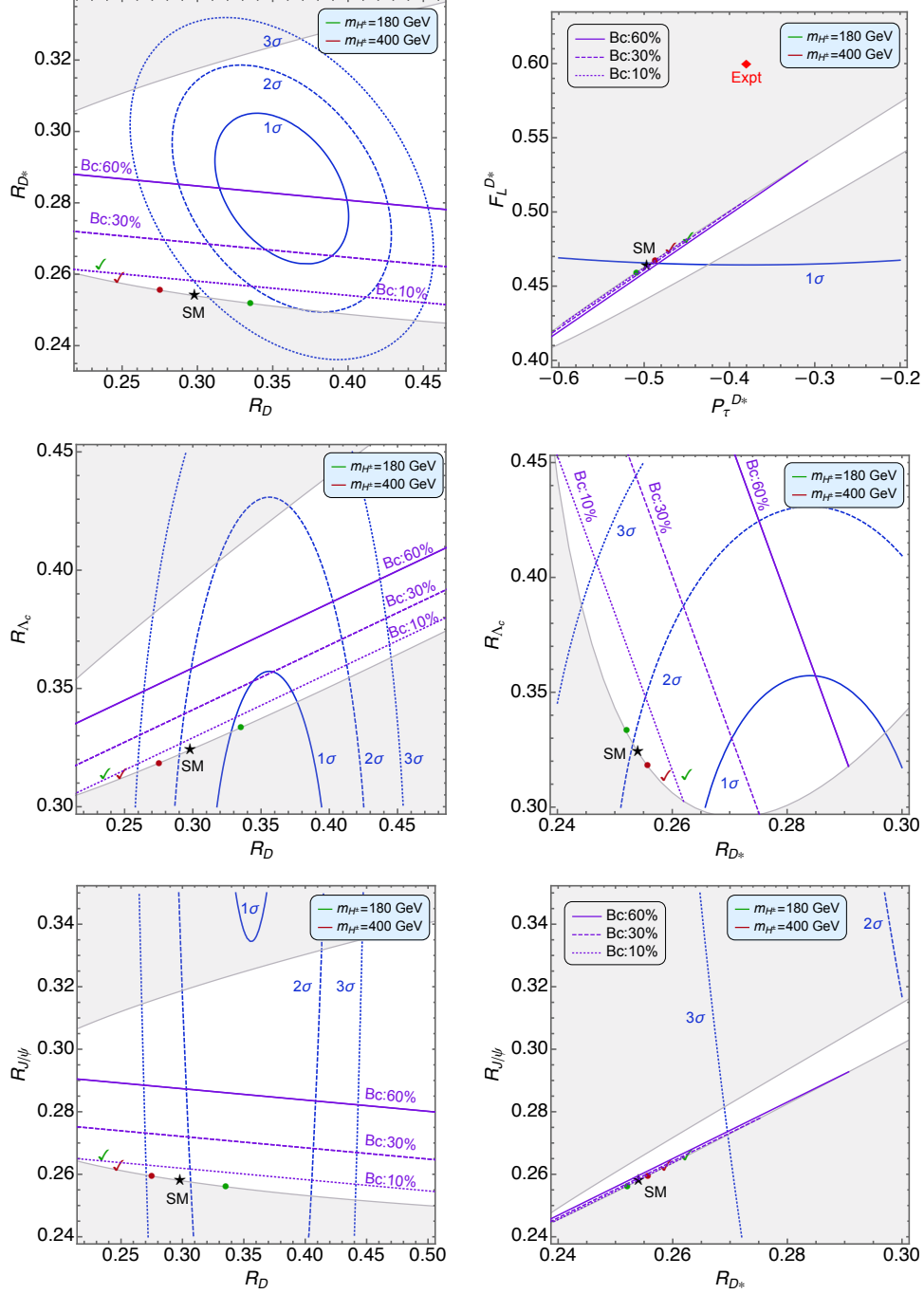


**Figure 14:** HL-LHC reach in  $\tau \nu$  and  $b \tau \nu$  final states to explain  $b \rightarrow \tau \nu$  anomalies. The benchmark points for the  $b$ -veto and  $b$ -tag categories are represented by dot and tick symbols, respectively, for  $m_{H^\pm} = 180$  and  $400$  GeV. The gray shaded region is not reachable considering the present model.

## 8 Summary and outlook

Experimental measurements of various flavor ratios, such as  $R_D$ ,  $R_{D^*}$ ,  $P_\tau^{D^*}$ ,  $F_L^{D^*}$ ,  $R_{J/\psi}$ , and  $R_{\Lambda_c}$ , corresponds to  $B \rightarrow D^{(*)}\tau\nu$ ,  $B_c \rightarrow J/\psi\tau\nu$ , and  $\Lambda_b \rightarrow \Lambda_c\tau\nu$  processes exhibit deviations from SM. If these deviations persist in future experiments, it would provide unequivocal evidence of physics beyond the scope of the SM.

In this study, we investigated these anomalies by considering an effective Lagrangian that incorporates the presence of new physics. Our primary objective is to determine the left-handed and right-handed scalar couplings by fitting the most recent experimental measurements of  $R_D$ ,  $R_{D^*}$ ,  $P_\tau^{D^*}$ ,  $F_L^{D^*}$ ,  $R_{J/\psi}$ , and  $R_{\Lambda_c}$ . We explored three best-fit scenarios, considering both real and complex scalar couplings in 1D scenario and complex scalar couplings in 2D scenario. We analyzed the impact of these fitted scalar couplings on various planes of flavor observables, including the  $R_D - R_{D^*}$ ,  $P_\tau^{D^*} - F_L^{D^*}$ ,  $R_D - R_{\Lambda_c}$ ,  $R_{D^*} - R_{\Lambda_c}$ ,  $R_D - R_{J/\psi}$ , and  $R_{D^*} - R_{J/\psi}$  planes. Furthermore, we take into account the upper bounds on  $\mathcal{B}(B_c \rightarrow \tau\nu) \leq 10\%$ ,  $30\%$ , and  $60\%$ . Our analysis reveal that complex scalar couplings provide better fits in the 1D scenario for most cases, but they tend to be located near or above the upper bound of  $\mathcal{B}(B_c \rightarrow \tau\nu) \leq 60\%$ . Conversely, the 2D scenario yields better results compared to the 1D fits.

A charged Higgs boson arising from a generic two Higgs doublet model, has been shown to provide a satisfactory explanation for the observed  $R_D - R_{D^*}$  anomaly [75, 76], given that its mass remains below 400 GeV. In this context, LHC serves as a promising platform for exploring the presence of these light scalar resonances and investigating potential new physics footprints in  $b \rightarrow c\tau\nu$  transitions. To search for these charged Higgs bosons, we have focused on two final states:  $pp \rightarrow H^\pm \rightarrow \tau\nu$  and  $pp \rightarrow bH^\pm \rightarrow b\tau\nu$ , at a center-of-mass energy of  $\sqrt{s} = 14$  TeV, with an integrated luminosity of  $3 \text{ ab}^{-1}$ . Our study involves a comprehensive collider analysis, wherein we optimize the selection cuts on various kinematic observables for a set of benchmark masses for the charged Higgs boson, specifically  $m_{H^\pm} = [180, 200, 250, 300, 350, 400]$  GeV. The  $pp \rightarrow bH^\pm \rightarrow b\tau\nu$  final state, also referred to as the b-tag category, exhibits lower contamination from the dominant  $W$ +jets background. Consequently, the addition of systematic uncertainties has a lesser impact on this channel. This advantage can be attributed to the additional requirement of b-tagging in the  $b\tau\nu$  final state, which aids in reducing background contributions.

The upper limits obtained for  $\sigma(pp \rightarrow bH^\pm \rightarrow b\tau\nu)$  impose a more stringent constraint on the  $(|y_{bc}|, |y_{\tau\nu}|)$  plane compared to the upper limits on  $\sigma(pp \rightarrow H^\pm \rightarrow \tau\nu)$ . By translating these limits into the planes of flavor observables, we observe that the HL-LHC has sensitivity to charged scalar effects in various regions: In the  $R_D - R_{D^*}$  plane, HL-LHC is sensitive in

nearly the entire  $3\sigma$  region. In the  $P_\tau^{D^*} - F_L^{D^*}$  plane, it covers the  $1\sigma - 2\sigma$  region of interest. HL-LHC can probe charged Higgs effects up to the  $3\sigma$  region in the  $R_D - R_{\Lambda_c}$  plane. In the  $R_{D^*} - R_{\Lambda_c}$  plane, it reaches sensitivity up to the  $2\sigma$  region. However, it covers a significant portion of the  $2\sigma - 3\sigma$  region in the  $R_D - R_{J/\psi}$  plane. In case of the  $R_{D^*} - R_{J/\psi}$  plane, HL-LHC can explore a small region up to the  $3\sigma$  level.

Indeed, these observations indicate that the HL-LHC has the potential to not only probe but also potentially exclude the existence of a charged Higgs boson in the low mass range. Furthermore, the HL-LHC can thoroughly investigate the anomalies observed in flavor observables associated with the  $b \rightarrow c\tau\nu$  transitions across multiple planes. By doing so, it can provide valuable insights into the underlying physics responsible for these flavor anomalies. The HL-LHC's capability to explore these phenomena offers a significant opportunity to deepen our understanding of flavor physics and potentially uncover new physics beyond the Standard Model.

## Acknowledgments

We would like to thank N. Rajeev, Girish Kumar, Syuhei Iguro, Biplob Bhattacharjee and Ayan Paul for helpful discussions throughout the course of this work. We would also like to thank Wolfgang Altmannshofer for the fruitful discussion on the topics addressed in this article. A.A. thanks the Planck conference, University of Warsaw for hospitality where discussions and part of this work was completed. A.A. acknowledges partial financial support from the Polish National Science Center under the Beethoven series grant number DEC-2016/23/G/ST2/04301. In the final stage of this project the research of A.A. has received funding from the Norwegian Financial Mechanism for years 2014-2021, grant nr DEC-2019/34/H/ST2/00707.

## A Detail of the generation cuts and production cross section of backgrounds

Process	Backgrounds	Generation-level cuts ( $\ell = e^\pm, \mu^\pm, \tau^\pm$ ) (NA : Not Applied)	Cross section (fb)
$\tau_h \nu$ / $b\tau_h \nu$	$t\bar{t}$ hadronic <sup>1</sup>	$p_{T,j/b} > 20$ GeV, $p_{T,\ell} > 15$ GeV, $ \eta_{j/b/\ell}  < 5.0$ , $\Delta R_{j,b,\ell} > 0.2$ , $\cancel{E}_T > 50$ GeV	199840.6
	$t\bar{t}$ semi-leptonic	same as $t\bar{t}$ hadronic	41051.6
	$t\bar{t}$ leptonic		5483.4
	W + jets		672182
	Misid. $\tau_h$		497287
	DY + jets		1584131.4
	ZZ + jets		12276.8
	WZ + jets		41286.5
	WW + jets		360887
	Single top Wt-channel		26489.8

**Table 9:** *The generation level cuts for various backgrounds used in the analyses along with the production cross-sections.*

---

<sup>1</sup>The  $t\bar{t}$  production cross-sections are taken at NNLO order [116].

## References

- [1] BABAR collaboration, J. P. Lees et al., *Evidence for an excess of  $\bar{B} \rightarrow D^{(*)}\tau^-\bar{\nu}_\tau$  decays*, *Phys. Rev. Lett.* **109** (2012) 101802, [[1205.5442](#)].
- [2] BABAR collaboration, J. P. Lees et al., *Measurement of an Excess of  $\bar{B} \rightarrow D^{(*)}\tau^-\bar{\nu}_\tau$  Decays and Implications for Charged Higgs Bosons*, *Phys. Rev. D* **88** (2013) 072012, [[1303.0571](#)].
- [3] BELLE collaboration, M. Huschle et al., *Measurement of the branching ratio of  $\bar{B} \rightarrow D^{(*)}\tau^-\bar{\nu}_\tau$  relative to  $\bar{B} \rightarrow D^{(*)}\ell^-\bar{\nu}_\ell$  decays with hadronic tagging at Belle*, *Phys. Rev. D* **92** (2015) 072014, [[1507.03233](#)].
- [4] BELLE collaboration, Y. Sato et al., *Measurement of the branching ratio of  $\bar{B}^0 \rightarrow D^{*+}\tau^-\bar{\nu}_\tau$  relative to  $\bar{B}^0 \rightarrow D^{*+}\ell^-\bar{\nu}_\ell$  decays with a semileptonic tagging method*, *Phys. Rev. D* **94** (2016) 072007, [[1607.07923](#)].
- [5] BELLE collaboration, G. Caria et al., *Measurement of  $\mathcal{R}(D)$  and  $\mathcal{R}(D^*)$  with a semileptonic tagging method*, *Phys. Rev. Lett.* **124** (2020) 161803, [[1910.05864](#)].
- [6] LHCb collaboration, R. Aaij et al., *Measurement of the ratio of branching fractions  $\mathcal{B}(\bar{B}^0 \rightarrow D^{*+}\tau^-\bar{\nu}_\tau)/\mathcal{B}(\bar{B}^0 \rightarrow D^{*+}\mu^-\bar{\nu}_\mu)$* , *Phys. Rev. Lett.* **115** (2015) 111803, [[1506.08614](#)].
- [7] LHCb collaboration, R. Aaij et al., *Measurement of the ratio of the  $B^0 \rightarrow D^{*-}\tau^+\nu_\tau$  and  $B^0 \rightarrow D^{*-}\mu^+\nu_\mu$  branching fractions using three-prong  $\tau$ -lepton decays*, *Phys. Rev. Lett.* **120** (2018) 171802, [[1708.08856](#)].
- [8] LHCb collaboration, R. Aaij et al., *Test of Lepton Flavor Universality by the measurement of the  $B^0 \rightarrow D^{*-}\tau^+\nu_\tau$  branching fraction using three-prong  $\tau$  decays*, *Phys. Rev. D* **97** (2018) 072013, [[1711.02505](#)].
- [9] LHCb collaboration, "First joint measurement of  $\mathcal{R}(D^*)$  and  $\mathcal{R}(D^0)$  at LHCb." <https://indico.cern.ch/event/1187939/>, .
- [10] [https://hflav-eos.web.cern.ch/hflav-eos/semi/winter23\\_prel/html/RDsDsstar/RDRDs.html](https://hflav-eos.web.cern.ch/hflav-eos/semi/winter23_prel/html/RDsDsstar/RDRDs.html).
- [11] LHCb collaboration, R. Aaij et al., *Measurement of the ratio of branching fractions  $\mathcal{B}(B_c^+ \rightarrow J/\psi\tau^+\nu_\tau)/\mathcal{B}(B_c^+ \rightarrow J/\psi\mu^+\nu_\mu)$* , *Phys. Rev. Lett.* **120** (2018) 121801, [[1711.05623](#)].
- [12] LHCb collaboration, R. Aaij et al., *Observation of the decay  $\Lambda_b^0 \rightarrow \Lambda_c^+\tau^-\bar{\nu}_\tau$* , *Phys. Rev. Lett.* **128** (2022) 191803, [[2201.03497](#)].
- [13] BELLE collaboration, S. Hirose et al., *Measurement of the  $\tau$  lepton polarization and  $\mathcal{R}(D^*)$  in the decay  $\bar{B} \rightarrow D^*\tau^-\bar{\nu}_\tau$* , *Phys. Rev. Lett.* **118** (2017) 211801, [[1612.00529](#)].
- [14] BELLE collaboration, S. Hirose et al., *Measurement of the  $\tau$  lepton polarization and  $\mathcal{R}(D^*)$  in the decay  $\bar{B} \rightarrow D^*\tau^-\bar{\nu}_\tau$  with one-prong hadronic  $\tau$  decays at Belle*, *Phys. Rev. D* **97** (2018) 012004, [[1709.00129](#)].
- [15] BELLE collaboration, A. Abdesselam et al., *Measurement of the  $D^{*-}$  polarization in the decay  $B^0 \rightarrow D^{*-}\tau^+\nu_\tau$* , in *10th International Workshop on the CKM Unitarity Triangle*, 3, 2019. [[1903.03102](#)].

- [16] R. Alonso, B. Grinstein and J. Martin Camalich, *Lifetime of  $B_c^-$  Constrains Explanations for Anomalies in  $B \rightarrow D^{(*)}\tau\nu$* , *Phys. Rev. Lett.* **118** (2017) 081802, [[1611.06676](#)].
- [17] C.-H. Chang, S.-L. Chen, T.-F. Feng and X.-Q. Li, *The Lifetime of  $B_c$  meson and some relevant problems*, *Phys. Rev. D* **64** (2001) 014003, [[hep-ph/0007162](#)].
- [18] M. Beneke and G. Buchalla, *The  $B_c$  Meson Lifetime*, *Phys. Rev. D* **53** (1996) 4991–5000, [[hep-ph/9601249](#)].
- [19] PARTICLE DATA GROUP collaboration, R. L. Workman et al., *Review of Particle Physics*, *PTEP* **2022** (2022) 083C01.
- [20] A. G. Akeroyd and C.-H. Chen, *Constraint on the branching ratio of  $B_c \rightarrow \tau\bar{\nu}$  from LEP1 and consequences for  $R(D^{(*)})$  anomaly*, *Phys. Rev. D* **96** (2017) 075011, [[1708.04072](#)].
- [21] M. Blanke, A. Crivellin, T. Kitahara, M. Moscati, U. Nierste and I. Nišandžić, *Addendum to “Impact of polarization observables and  $B_c \rightarrow \tau\nu$  on new physics explanations of the  $b \rightarrow c\tau\nu$  anomaly”*, [1905.08253](#).
- [22] Y. Sakaki and H. Tanaka, *Constraints on the charged scalar effects using the forward-backward asymmetry on  $B^- \rightarrow D^{(*)}\tau\nu^- \tau$* , *Phys. Rev. D* **87** (2013) 054002, [[1205.4908](#)].
- [23] S. Fajfer, J. F. Kamenik, I. Nisandzic and J. Zupan, *Implications of Lepton Flavor Universality Violations in  $B$  Decays*, *Phys. Rev. Lett.* **109** (2012) 161801, [[1206.1872](#)].
- [24] A. Datta, M. Duraisamy and D. Ghosh, *Diagnosing New Physics in  $b \rightarrow c\tau\nu_\tau$  decays in the light of the recent BaBar result*, *Phys. Rev. D* **86** (2012) 034027, [[1206.3760](#)].
- [25] D. Bečirević, N. Košnik and A. Tayduganov,  *$\bar{B} \rightarrow D\tau\bar{\nu}_\tau$  vs.  $\bar{B} \rightarrow D\mu\bar{\nu}_\mu$* , *Phys. Lett. B* **716** (2012) 208–213, [[1206.4977](#)].
- [26] M. Tanaka and R. Watanabe, *New physics in the weak interaction of  $\bar{B} \rightarrow D^{(*)}\tau\bar{\nu}$* , *Phys. Rev. D* **87** (2013) 034028, [[1212.1878](#)].
- [27] M. Duraisamy and A. Datta, *The Full  $B \rightarrow D^*\tau^-\bar{\nu}_\tau$  Angular Distribution and CP violating Triple Products*, *JHEP* **09** (2013) 059, [[1302.7031](#)].
- [28] R. Dutta, A. Bhol and A. K. Giri, *Effective theory approach to new physics in  $b \rightarrow u$  and  $b \rightarrow c$  leptonic and semileptonic decays*, *Phys. Rev. D* **88** (2013) 114023, [[1307.6653](#)].
- [29] M. Duraisamy, P. Sharma and A. Datta, *Azimuthal  $B \rightarrow D^*\tau^-\bar{\nu}_\tau$  angular distribution with tensor operators*, *Phys. Rev. D* **90** (2014) 074013, [[1405.3719](#)].
- [30] Y. Sakaki, M. Tanaka, A. Tayduganov and R. Watanabe, *Probing New Physics with  $q^2$  distributions in  $\bar{B} \rightarrow D^{(*)}\tau\bar{\nu}$* , *Phys. Rev. D* **91** (2015) 114028, [[1412.3761](#)].
- [31] M. Freytsis, Z. Ligeti and J. T. Ruderman, *Flavor models for  $\bar{B} \rightarrow D^{(*)}\tau\bar{\nu}$* , *Phys. Rev. D* **92** (2015) 054018, [[1506.08896](#)].
- [32] A. K. Alok, D. Kumar, S. Kumbhakar and S. U. Sankar,  *$D^*$  polarization as a probe to discriminate new physics in  $\bar{B} \rightarrow D^*\tau\bar{\nu}$* , *Phys. Rev. D* **95** (2017) 115038, [[1606.03164](#)].

- [33] R. Alonso, A. Kobach and J. Martin Camalich, *New physics in the kinematic distributions of  $\bar{B} \rightarrow D^{(*)}\tau^-(\rightarrow \ell^-\bar{\nu}_\ell\nu_\tau)\bar{\nu}_\tau$* , *Phys. Rev. D* **94** (2016) 094021, [[1602.07671](#)].
- [34] D. Bardhan, P. Byakti and D. Ghosh, *A closer look at the  $R_D$  and  $R_{D^*}$  anomalies*, *JHEP* **01** (2017) 125, [[1610.03038](#)].
- [35] S. Bhattacharya, S. Nandi and S. K. Patra, *Looking for possible new physics in  $B \rightarrow D^{(*)}\tau\nu_\tau$  in light of recent data*, *Phys. Rev. D* **95** (2017) 075012, [[1611.04605](#)].
- [36] A. Celis, M. Jung, X.-Q. Li and A. Pich, *Scalar contributions to  $b \rightarrow c(u)\tau\nu$  transitions*, *Phys. Lett. B* **771** (2017) 168–179, [[1612.07757](#)].
- [37] R. Dutta, *Exploring  $R_D$ ,  $R_{D^*}$  and  $R_{J/\Psi}$  anomalies*, [1710.00351](#).
- [38] A. K. Alok, D. Kumar, J. Kumar, S. Kumbhakar and S. U. Sankar, *New physics solutions for  $R_D$  and  $R_{D^*}$* , *JHEP* **09** (2018) 152, [[1710.04127](#)].
- [39] A. Azatov, D. Bardhan, D. Ghosh, F. Sgarlata and E. Venturini, *Anatomy of  $b \rightarrow c\tau\nu$  anomalies*, *JHEP* **11** (2018) 187, [[1805.03209](#)].
- [40] S. Bhattacharya, S. Nandi and S. Kumar Patra,  *$b \rightarrow c\tau\nu_\tau$  Decays: a catalogue to compare, constrain, and correlate new physics effects*, *Eur. Phys. J. C* **79** (2019) 268, [[1805.08222](#)].
- [41] F. Feruglio, P. Paradisi and O. Sumensari, *Implications of scalar and tensor explanations of  $R_{D^{(*)}}$* , *JHEP* **11** (2018) 191, [[1806.10155](#)].
- [42] Z.-R. Huang, Y. Li, C.-D. Lu, M. A. Paracha and C. Wang, *Footprints of New Physics in  $b \rightarrow c\tau\nu$  Transitions*, *Phys. Rev. D* **98** (2018) 095018, [[1808.03565](#)].
- [43] A. Angelescu, D. Bećirević, D. A. Faroughy and O. Sumensari, *Closing the window on single leptoquark solutions to the  $B$ -physics anomalies*, *JHEP* **10** (2018) 183, [[1808.08179](#)].
- [44] S. Bifani, S. Descotes-Genon, A. Romero Vidal and M.-H. Schune, *Review of Lepton Universality tests in  $B$  decays*, *J. Phys. G* **46** (2019) 023001, [[1809.06229](#)].
- [45] Q.-Y. Hu, X.-Q. Li and Y.-D. Yang,  *$b \rightarrow c\tau\nu$  transitions in the standard model effective field theory*, *Eur. Phys. J. C* **79** (2019) 264, [[1810.04939](#)].
- [46] S. Iguro, Y. Omura and M. Takeuchi, *Test of the  $R(D^{(*)})$  anomaly at the LHC*, *Phys. Rev. D* **99** (2019) 075013, [[1810.05843](#)].
- [47] P. Asadi, M. R. Buckley and D. Shih, *Asymmetry Observables and the Origin of  $R_{D^{(*)}}$  Anomalies*, *Phys. Rev. D* **99** (2019) 035015, [[1810.06597](#)].
- [48] R. Dutta and N. Rajeev, *Signature of lepton flavor universality violation in  $B_s \rightarrow D_s\tau\nu$  semileptonic decays*, *Phys. Rev. D* **97** (2018) 095045, [[1803.03038](#)].
- [49] N. Rajeev and R. Dutta, *Impact of vector new physics couplings on  $B_s \rightarrow (K, K^*)\tau\nu$  and  $B \rightarrow \pi\tau\nu$  decays*, *Phys. Rev. D* **98** (2018) 055024, [[1808.03790](#)].
- [50] J. Aebischer, J. Kumar, P. Stangl and D. M. Straub, *A Global Likelihood for Precision Constraints and Flavour Anomalies*, *Eur. Phys. J. C* **79** (2019) 509, [[1810.07698](#)].

- [51] C. Murgui, A. Peñuelas, M. Jung and A. Pich, *Global fit to  $b \rightarrow c\tau\nu$  transitions*, *JHEP* **09** (2019) 103, [[1904.09311](#)].
- [52] R.-X. Shi, L.-S. Geng, B. Grinstein, S. Jäger and J. Martin Camalich, *Revisiting the new-physics interpretation of the  $b \rightarrow c\tau\nu$  data*, *JHEP* **12** (2019) 065, [[1905.08498](#)].
- [53] N. Rajeev, R. Dutta and S. Kumbhakar, *Implication of  $R_{D^{(*)}}$  anomalies on semileptonic decays of  $\Sigma_b$  and  $\Omega_b$  baryons*, *Phys. Rev. D* **100** (2019) 035015, [[1905.13468](#)].
- [54] N. Das and R. Dutta, *Implication of  $b \rightarrow c\tau\nu$  flavor anomalies on  $B_s \rightarrow D_s^*\tau\nu$  decay observables*, *J. Phys. G* **47** (2020) 115001, [[1912.06811](#)].
- [55] N. Das and R. Dutta, *New physics footprints in the angular distribution of  $B_s \rightarrow D_s^*(\rightarrow D_s\gamma, D_s\pi)\tau\nu$  decays*, *Phys. Rev. D* **105** (2022) 055027, [[2110.05526](#)].
- [56] D. Bečirević, M. Fedele, I. Nišandžić and A. Tayduganov, *Lepton Flavor Universality tests through angular observables of  $\bar{B} \rightarrow D^{(*)}\ell\bar{\nu}$  decay modes*, [[1907.02257](#)].
- [57] D. Bečirević, F. Jaffredo, A. Peñuelas and O. Sumensari, *New Physics effects in leptonic and semileptonic decays*, *JHEP* **05** (2021) 175, [[2012.09872](#)].
- [58] T. P. Cheng and M. Sher, *Mass-matrix ansatz and flavor nonconservation in models with multiple higgs doublets*, *Phys. Rev. D* **35** (Jun, 1987) 3484–3491.
- [59] G. C. Branco, P. M. Ferreira, L. Lavoura, M. N. Rebelo, M. Sher and J. P. Silva, *Theory and phenomenology of two-Higgs-doublet models*, *Phys. Rept.* **516** (2012) 1–102, [[1106.0034](#)].
- [60] A. Crivellin, C. Greub and A. Kokulu, *Explaining  $B \rightarrow D\tau\nu$ ,  $B \rightarrow D^*\tau\nu$  and  $B \rightarrow \tau\nu$  in a 2HDM of type III*, *Phys. Rev. D* **86** (2012) 054014, [[1206.2634](#)].
- [61] A. Celis, M. Jung, X.-Q. Li and A. Pich, *Sensitivity to charged scalars in  $B \rightarrow D^{(*)}\tau\nu_\tau$  and  $B \rightarrow \tau\nu_\tau$  decays*, *JHEP* **01** (2013) 054, [[1210.8443](#)].
- [62] P. Ko, Y. Omura and C. Yu,  *$B \rightarrow D^{(*)}\tau\nu$  and  $B \rightarrow \tau\nu$  in chiral  $U(1)'$  models with flavored multi Higgs doublets*, *JHEP* **03** (2013) 151, [[1212.4607](#)].
- [63] A. Crivellin, A. Kokulu and C. Greub, *Flavor-phenomenology of two-Higgs-doublet models with generic Yukawa structure*, *Phys. Rev. D* **87** (2013) 094031, [[1303.5877](#)].
- [64] A. Crivellin, J. Heeck and P. Stoffer, *A perturbed lepton-specific two-Higgs-doublet model facing experimental hints for physics beyond the Standard Model*, *Phys. Rev. Lett.* **116** (2016) 081801, [[1507.07567](#)].
- [65] C. S. Kim, Y. W. Yoon and X.-B. Yuan, *Exploring top quark FCNC within 2HDM type III in association with flavor physics*, *JHEP* **12** (2015) 038, [[1509.00491](#)].
- [66] J. M. Cline, *Scalar doublet models confront  $\tau$  and  $b$  anomalies*, *Phys. Rev. D* **93** (2016) 075017, [[1512.02210](#)].
- [67] J.-P. Lee,  *$B \rightarrow D^{(*)}\tau\nu_\tau$  in the 2HDM with an anomalous  $\tau$  coupling*, *Phys. Rev. D* **96** (2017) 055005, [[1705.02465](#)].



- [68] S. Iguro and K. Tobe,  $R(D^{(*)})$  in a general two Higgs doublet model, *Nucl. Phys. B* **925** (2017) 560–606, [[1708.06176](#)].
- [69] S. Iguro and Y. Omura, Status of the semileptonic  $B$  decays and muon  $g-2$  in general 2HDMs with right-handed neutrinos, *JHEP* **05** (2018) 173, [[1802.01732](#)].
- [70] C.-H. Chen and T. Nomura, Charged Higgs boson contribution to  $B_q^- \rightarrow \ell \bar{\nu}$  and  $\bar{B} \rightarrow (P, V)\ell \bar{\nu}$  in a generic two-Higgs doublet model, *Phys. Rev. D* **98** (2018) 095007, [[1803.00171](#)].
- [71] R. Martinez, C. F. Sierra and G. Valencia, Beyond  $\mathcal{R}(D^{(*)})$  with the general type-III 2HDM for  $b \rightarrow c\tau\nu$ , *Phys. Rev. D* **98** (2018) 115012, [[1805.04098](#)].
- [72] S.-P. Li, X.-Q. Li, Y.-D. Yang and X. Zhang,  $R_{D^{(*)}}, R_{K^{(*)}}$  and neutrino mass in the 2HDM-III with right-handed neutrinos, *JHEP* **09** (2018) 149, [[1807.08530](#)].
- [73] J. Cardozo, J. H. Muñoz, N. Quintero and E. Rojas, Analysing the charged scalar boson contribution to the charged-current  $B$  meson anomalies, *J. Phys. G* **48** (2021) 035001, [[2006.07751](#)].
- [74] P. Athron, C. Balazs, T. E. Gonzalo, D. Jacob, F. Mahmoudi and C. Sierra, Likelihood analysis of the flavour anomalies and  $g - 2$  in the general two Higgs doublet model, *JHEP* **01** (2022) 037, [[2111.10464](#)].
- [75] S. Iguro, Revival of  $H^-$  interpretation of  $RD^{(*)}$  anomaly and closing low mass window, *Phys. Rev. D* **105** (2022) 095011, [[2201.06565](#)].
- [76] M. Blanke, S. Iguro and H. Zhang, Towards ruling out the charged Higgs interpretation of the  $R_{D^{(*)}}$  anomaly, *JHEP* **06** (2022) 043, [[2202.10468](#)].
- [77] G. Kumar, Interplay of the charged Higgs boson effects in  $R_{D^{(*)}}$ ,  $b \rightarrow s\ell^+\ell^-$ , and  $W$  mass, *Phys. Rev. D* **107** (2023) 075016, [[2212.07233](#)].
- [78] T. Miki, T. Miura and M. Tanaka, Effects of charged Higgs boson and QCD corrections in  $\text{anti-}B \rightarrow D \tau \text{ anti-}\nu(\tau)$ , in *3rd Workshop on Higher Luminosity B Factory*, pp. 116–124, 10, 2002. [hep-ph/0210051](#).
- [79] A. Wahab El Kaffas, P. Osland and O. M. Ogreid, Constraining the Two-Higgs-Doublet-Model parameter space, *Phys. Rev. D* **76** (2007) 095001, [[0706.2997](#)].
- [80] O. Deschamps, S. Descotes-Genon, S. Monteil, V. Niess, S. T’Jampens and V. Tisserand, The Two Higgs Doublet of Type II facing flavour physics data, *Phys. Rev. D* **82** (2010) 073012, [[0907.5135](#)].
- [81] T. Bhattacharya, V. Cirigliano, S. D. Cohen, A. Filipuzzi, M. Gonzalez-Alonso, M. L. Graesser et al., Probing Novel Scalar and Tensor Interactions from (Ultra)Cold Neutrons to the LHC, *Phys. Rev. D* **85** (2012) 054512, [[1110.6448](#)].
- [82] V. Cirigliano, J. Jenkins and M. Gonzalez-Alonso, Semileptonic decays of light quarks beyond the Standard Model, *Nucl. Phys. B* **830** (2010) 95–115, [[0908.1754](#)].
- [83] S. Iguro, T. Kitahara and R. Watanabe, Global fit to  $b \rightarrow c\tau\nu$  anomalies 2022 mid-autumn, [2210.10751](#).

- [84] R. Mandal, C. Murgui, A. Peñuelas and A. Pich, *The role of right-handed neutrinos in  $b \rightarrow c\tau\bar{\nu}$  anomalies*, *JHEP* **08** (2020) 022, [[2004.06726](#)].
- [85] M. Blanke, A. Crivellin, S. de Boer, T. Kitahara, M. Moscati, U. Nierste et al., *Impact of polarization observables and  $B_c \rightarrow \tau\nu$  on new physics explanations of the  $b \rightarrow c\tau\nu$  anomaly*, *Phys. Rev. D* **99** (2019) 075006, [[1811.09603](#)].
- [86] MILC collaboration, J. A. Bailey et al.,  *$B \rightarrow D\ell\nu$  form factors at nonzero recoil and  $-V_{cb}$  from 2+1-flavor lattice QCD*, *Phys. Rev. D* **92** (2015) 034506, [[1503.07237](#)].
- [87] HPQCD collaboration, J. Harrison, C. T. H. Davies and A. Lytle,  *$B_c \rightarrow J/\psi$  form factors for the full  $q^2$  range from lattice QCD*, *Phys. Rev. D* **102** (2020) 094518, [[2007.06957](#)].
- [88] I. Caprini, L. Lellouch and M. Neubert, *Dispersive bounds on the shape of anti- $B \rightarrow D^{(*)}$  lepton anti-neutrino form-factors*, *Nucl. Phys. B* **530** (1998) 153–181, [[hep-ph/9712417](#)].
- [89] W. Detmold, C. Lehner and S. Meinel,  *$\Lambda_b \rightarrow p\ell^-\bar{\nu}_\ell$  and  $\Lambda_b \rightarrow \Lambda_c\ell^-\bar{\nu}_\ell$  form factors from lattice QCD with relativistic heavy quarks*, *Phys. Rev. D* **92** (2015) 034503, [[1503.01421](#)].
- [90] F. James and M. Roos, *Minuit - a system for function minimization and analysis of the parameter errors and correlations*, *Computer Physics Communications* **10** (1975) 343–367.
- [91] H. Dembinski, P. Ongmongkolkul, C. Deil, H. Schreiner, M. Feickert, Andrew et al., *scikit-hep/iminuit: v*, Feb., 2023. 10.5281/zenodo.7630430.
- [92] HPQCD collaboration, H. Na, C. M. Bouchard, G. P. Lepage, C. Monahan and J. Shigemitsu,  *$B \rightarrow D\ell\nu$  form factors at nonzero recoil and extraction of  $|V_{cb}|$* , *Phys. Rev. D* **92** (2015) 054510, [[1505.03925](#)].
- [93] S. Aoki et al., *Review of lattice results concerning low-energy particle physics*, *Eur. Phys. J. C* **77** (2017) 112, [[1607.00299](#)].
- [94] D. Bigi and P. Gambino, *Revisiting  $B \rightarrow D\ell\nu$* , *Phys. Rev. D* **94** (2016) 094008, [[1606.08030](#)].
- [95] BELLE collaboration, A. Abdesselam et al., *Measurement of  $\mathcal{R}(D)$  and  $\mathcal{R}(D^*)$  with a semileptonic tagging method*, [[1904.08794](#)].
- [96] F. U. Bernlochner, Z. Ligeti, M. Papucci and D. J. Robinson, *Combined analysis of semileptonic  $B$  decays to  $D$  and  $D^*$ :  $R(D^{(*)})$ ,  $|V_{cb}|$ , and new physics*, *Phys. Rev. D* **95** (2017) 115008, [[1703.05330](#)].
- [97] S. Jaiswal, S. Nandi and S. K. Patra, *Extraction of  $|V_{cb}|$  from  $B \rightarrow D^{(*)}\ell\nu_\ell$  and the Standard Model predictions of  $R(D^{(*)})$* , *JHEP* **12** (2017) 060, [[1707.09977](#)].
- [98] S. Fajfer, J. F. Kamenik and I. Nisandzic, *On the  $B \rightarrow D^*\tau\bar{\nu}_\tau$  Sensitivity to New Physics*, *Phys. Rev. D* **85** (2012) 094025, [[1203.2654](#)].
- [99] D. Bigi, P. Gambino and S. Schacht,  *$R(D^*)$ ,  $|V_{cb}|$ , and the Heavy Quark Symmetry relations between form factors*, *JHEP* **11** (2017) 061, [[1707.09509](#)].
- [100] LATTICE-HPQCD collaboration, J. Harrison, C. T. H. Davies and A. Lytle,  *$R(J/\psi)$  and  $B_c^- \rightarrow J/\psi\ell^-\bar{\nu}_\ell$  Lepton Flavor Universality Violating Observables from Lattice QCD*, *Phys. Rev. Lett.* **125** (2020) 222003, [[2007.06956](#)].

- [101] T. D. Cohen, H. Lamm and R. F. Lebed, *Model-independent bounds on  $R(J/\psi)$* , *JHEP* **09** (2018) 168, [[1807.02730](#)].
- [102] F. U. Bernlochner, Z. Ligeti, D. J. Robinson and W. L. Sutcliffe, *Precise predictions for  $\Lambda_b \rightarrow \Lambda_c$  semileptonic decays*, *Phys. Rev. D* **99** (2019) 055008, [[1812.07593](#)].
- [103] P. D. Group, P. A. Zyla, R. M. Barnett, J. Beringer, O. Dahl, D. A. Dwyer et al., *Review of Particle Physics*, *Progress of Theoretical and Experimental Physics* **2020** (08, 2020) .
- [104] CMS collaboration, *Search for new physics in the  $\tau$  lepton plus missing transverse momentum final state in proton-proton collisions at  $\sqrt{s} = 13$  TeV*, [2212.12604](#).
- [105] CMS collaboration, A. M. Sirunyan et al., *Search for a  $W'$  boson decaying to a  $\tau$  lepton and a neutrino in proton-proton collisions at  $\sqrt{s} = 13$  TeV*, *Phys. Lett. B* **792** (2019) 107–131, [[1807.11421](#)].
- [106] J. Alwall, R. Frederix, S. Frixione, V. Hirschi, F. Maltoni, O. Mattelaer et al., *The automated computation of tree-level and next-to-leading order differential cross sections, and their matching to parton shower simulations*, *JHEP* **07** (2014) 079, [[1405.0301](#)].
- [107] T. Sjöstrand, S. Ask, J. R. Christiansen, R. Corke, N. Desai, P. Ilten et al., *An introduction to PYTHIA 8.2*, *Comput. Phys. Commun.* **191** (2015) 159–177, [[1410.3012](#)].
- [108] *ATLAS Run 1 Pythia8 tunes*, Tech. Rep. ATL-PHYS-PUB-2014-021, CERN, Geneva, Nov, 2014.
- [109] NNPDF collaboration, R. D. Ball et al., *Parton distributions for the LHC Run II*, *JHEP* **04** (2015) 040, [[1410.8849](#)].
- [110] M. Cacciari, G. P. Salam and G. Soyez, *FastJet User Manual*, *Eur. Phys. J. C* **72** (2012) 1896, [[1111.6097](#)].
- [111] M. Cacciari, G. P. Salam and G. Soyez, *The Anti- $k(t)$  jet clustering algorithm*, *JHEP* **04** (2008) 063, [[0802.1189](#)].
- [112] DELPHES 3 collaboration, J. de Favereau, C. Delaere, P. Demin, A. Giammanco, V. Lemaître, A. Mertens et al., *DELPHES 3, A modular framework for fast simulation of a generic collider experiment*, *JHEP* **02** (2014) 057, [[1307.6346](#)].
- [113] M. L. Mangano, M. Moretti, F. Piccinini and M. Treccani, *Matching matrix elements and shower evolution for top-quark production in hadronic collisions*, *JHEP* **01** (2007) 013, [[hep-ph/0611129](#)].
- [114] D. Marzocca, U. Min and M. Son, *Bottom-Flavored Mono-Tau Tails at the LHC*, *JHEP* **12** (2020) 035, [[2008.07541](#)].
- [115] L. Di Luzio, M. Kirk, A. Lenz and T. Rauh,  *$\Delta M_s$  theory precision confronts flavour anomalies*, *JHEP* **12** (2019) 009, [[1909.11087](#)].
- [116] <https://twiki.cern.ch/twiki/bin/view/LHCPhysics/TtbarNNLO>.